The Neoproterozoic Homrit Akarem Granitic Intrusion and the post-collisional rare-metal granites of the south Eastern Desert of Egypt

Bassam A. Abuamarah[a*], Mokhles K. Azer[b], Amany M. A. Seddik[c], Paul D. Asimow[d], Mahmoud H. Darwish[c], Pedro Guzman[e], Brent T. Fultz[e], M. J. Wilner[d], and Nathan Dalleska[d]

[a] *Department of Geology and Geophysics, King Saud University, Riyadh 11451, Saudi Arabia*
[b] *Geological Sciences Department, National Research Centre, Cairo, Egypt*
[c] *Geology Department, Faculty of Science, New Valley University, El-Kharga, 72511 Egypt*
[d] *Division of Geological & Planetary Sciences, California Institute of Technology, Pasadena CA 91125 USA*
[d] *Division of Engineering & Applied Sciences, California Institute of Technology, Pasadena CA 91125 USA*

Abstract

The Homrit Akarem granitic intrusion (HAGI) outcrops near the western edge of the south Easern Desert basement exposure in Egypt. It is a composite of two cogenetic intrusive bodies: an early albite granite phase shallowly emplaced at the apex of a magmatic cupola, and a later subjacent pink granite phase with better preservation of magmatic features. Mineral chemistry of primary biotite and garnet, together with whole-rock chemistry, identify the HAGI as a highly fractionated A-type peraluminous intrusion. The chemistry of F-dominant, Li-bearing, Fe^{3+}-rich primary magmatic mica in the pink granite resembles that typically found in highly evolved Nb-Y-F pegmatites. The HAGI is the evolved product of a primary magma generated by partial melting of juvenile ANS crust and emplaced along a regional strike-slip fault system that promoted its ascent. The main emplacement mechanism and evolutionary sequence of the HAGI was magmatic, although secondary minerals and textures resulting from hydrothermal fluid interactions are observed, especially at its margins. Primary columbite-(Mn) crystallized from melt and was partly replaced by secondary fluorcalciomicrolite. The high fluorine content of magmatic fluids exsolved from the intrusion is indicated by quartz-fluorite veins, greisenization, albitization, and F-bearing secondary oxide minerals. The magmatic derivation of this fluid is demonstrated by the F-dominant primary mica, a siderophyllite-polylithionite solid solution commonly known as zinnwaldite. The chemistry of zinnwaldite constrains the F/OH activity ratio and oxygen fugacity of its parental melt and thereby resolves the ambiguity between pressure and the effects of F in controlling the

[*] **Corresponding author:** Dr. Bassam A. Abuamarah (babuamarah@ksu.edu.sa)

normative quartz content of rare-metal granites. The HAGI is less mineralized than the post-collisional rare-metal granites found further east in the south Eastern Desert, replicating a trend observed previously in the central Eastern Desert and suggesting that east-west zoning in rare metal enrichment is a persistent feature across latitudes at the western edge of the ANS.

Keywords: Arabian-Nubian Shield, magmatic cupola, post-collisional, Nb–Ta oxides, Magmatic–hydrothermal evolution.

1. Introduction

The Homrit Akarem granitic intrusion (HAGI) outcrops in the southern part of the Eastern Desert of Egypt, the northwestern corner of the Arabian-Nubian Shield (ANS). The ANS is a large tract of juvenile continental crust (Meert, 2003; Johnson, 2003; Stoeser and Frost, 2006; Ali et al., 2010) that formed in Neoproterozoic time (850-590 Ma) as a result of the collision between East and West Gondwana during the extensive Pan-African orogeny (Stern, 1994; Rino et al., 2008). The ANS formed mostly by accretion of oceanic island-arc terranes that developed within or on the margins of the Mozambique Ocean between ~1000 and 640 Ma (Hargrove et al., 2006; Be'eri-Shlevin et al., 2009, 2011; Liégeois and Stern, 2010; Ali et al., 2010; Johnson et al., 2013), followed by extensive and voluminous intrusion and eruption of post-collisional magmatic series.

One of the most striking features of the ANS is the abundance of granitoid intrusions. They have various ages (~820 to 590 Ma), tectonic settings (syn-, late-, and post-orogenic) and magma types (calc-alkaline to alkaline/peralkaline) (e.g., Azer 2007; Moghazi et al., 2011, 2015; Khalil et al. 2018; Abuamarah, 2020; Azer et al., 2019, Azer and Asimow, 2020). The post-collisional granitic intrusions (610-590 Ma) are the most abundant. These plutons have attracted the attention of many authors due to their economic value and their potential as sources of strategic metals, including Nb, Ta, REE, U, Zr, and Th (e.g., Hackett, 1986; Helba et al., 1997; Küster, 2009; Moufti et al., 2013; Abdallah et al., 2020; Abuamarah et al., 2021; Seddik et al., 2020). Despite numerous published studies, the origins and geotectonic implications of the post-collisional granites of the ANS are still controversial. Among the notable unresolved questions are (1) the extent to which the low normative quartz content of these granitoids compared to the low-pressure H_2O-saturated granite minimum is attributable to high-pressure fractionation (e.g. Gualda and Ghiorso, 2014) or

to the effects of magmatic fluorine (Manning, 1981); (2) whether there are any tectonic predictors or geographical patterns within and among post-orogenic terranes in the degree of rare-metal enrichment and mineralization; and (3) the relative importance of magmatic and post-magmatic processes in transporting rare metals and concentrating them into ore bodies.

The HAGI is typical in many ways of the rare-metal bearing post-collisional granites in the Eastern Desert of Egypt and published work concerning the HAGI embodies many of the contradictory interpretations that have been assigned to these rocks (e.g., Hassanen et al., 1995; Hassanen and Harraz, 1996; Abd El-Naby et al., 2000; Mohamed et al., 2009; Ali et al., 2012). In this work, we integrate field work, petrography, mineral chemistry, and whole-rock geochemical analyses to discern the petrological characteristics, magmatic evolution and post-magmatic processes that affected the intrusion. This study offers a good opportunity to understand the petrogenetic processes leading to the formation of mineralized post-collisional granites throughout the ANS and elsewhere. During the present study, we examined the following key questions including (1) whether the intrusion represents one or multiple magmatic pulses, (2) what are the relative roles of magmatic and metasomatic processes in the differentiation of the HAGI and enrichment of associated ore deposits, (3) the use of F-rich mica species for quantitative F/OH estimation of the parental magma, (4) quantitative Fe^{3+}/Fe^{T} of the mica species as an oxybarometer, and (5) whether the geographic location and geochemistry of the HAGI contribute to defining an overall pattern in the rare metal mineralization of the ANS. We present a simplified tectono-magmatic model for the evolution of the HAGI. Finally, we discuss the implications of our results for the formation of juvenile continental crust — a key terrestrial process for which the ANS is one of the best natural laboratories.

2. Geologic setting and field observations

The distribution of the most important rare-metal bearing granite intrusions in the Eastern Desert of Egypt is shown in **Fig. 1a.** The HAGI (No. 13 in **Fig. 1a**) is one of only a few such intrusions in the southern part of the Eastern Desert and sits relatively far inland, ~140 km west of the Red Sea coast. It lies between latitudes 24° 10’ 00” and 24° 12’ 15” N and longitudes 34° 01’ 45” and 34° 05’ 30” E. The intrusion appears in satellite imagery as an elongated NE-SW semi-triangular main mass (~7 km^2) and a smaller elliptical (elongated E-W) satellite mass (~1 km^2) to

93 the east. The two masses are separated by a wadi, a mapped fault, and a sliver of country rock **(Fig.**
94 **1b)**. Exposed rock units in the Homrit Akarem area include a metamorphosed volcano-sedimentary
95 succession, two granitoid intrusive units, and Neogene wadi deposits **(Fig. 1c)**. The field
96 relationships between the different rock types of the Homrit Akarem intrusion and its country rocks
97 are shown in a schematic cross-section in **Fig. 1d.** The metamorphosed volcano-sedimentary rocks
98 belong to the island-arc stage of crustal evolution in the Eastern Desert of Egypt. They are the
99 oldest units in the mapped area; they are highly deformed and display some lineation. The intrusive
100 granitoids in the study area include a granodiorite unit (with minor tonalite) and the Homrit Akarem
101 granite intrusion. Both are intruded into the metamorphosed volcano-sedimentary island-arc
102 sequence; there is no contact between the two intrusions in outcrop.
103 The granodiorite occupies the northwestern part of the mapped area. It is medium- to
104 coarse-grained, greyish-green to whitish-green, and contains xenoliths of the metasedimentary
105 country rock **(Fig 2a)**. The HAGI represents the youngest igneous activity in the area, with sharp
106 intrusive contacts against the metamorphosed volcano-sedimentary rocks **(Fig. 2b)** marked locally
107 by a thin (0.5-1 m) hornfelsic contact metamorphic aureole around the intrusion.
108 Based on field observations, we divide the HAGI itself into pink granite, muscovite granite
109 and albite granite. The contacts between the different phases of the pluton may be sharp or
110 gradational; in weathered areas the subunits and their contacts are difficult to discern. In the field,
111 the pink granite is a massive, coarse-grained, homogenous rock forming the core of the pluton. It
112 grades laterally outwards into muscovite granite along the margins and vertically upwards into
113 whitish albite granite. A few granodioritic xenoliths are observed in the marginal muscovite granite
114 phase **(Fig. 2c)**. The albite granite occupies the apical portion of the pluton **(Fig. 2d)**. It is fine- to
115 medium-grained and whitish in color with bleached appearance and seriate to porphyritic texture.
116 Some parts of both masses of the intrusion are highly tectonized and broken by numerous fractures
117 trending NW-SE and NE-SW **(Fig. 2f)**.
118 Toward the outer margins of the HAGI, the granites and their country rocks host numerous
119 dykes and veins of pegmatite, greisen, fluorite and quartz. Greisens of both pervasive and vein type
120 are erratically distributed around the margins of the HAGI. Some greisen pockets are mineralized
121 and contain appreciable amounts of cassiterite. Quartz-fluorite veins are common on the northern
122 and the eastern margins of the pluton and occur as discontinuous lenses and veins 10-50 cm wide

and up to several hundred meters long. Many of the quartz veins invaded the metasedimentary country rocks, especially in the eastern part of the mapped area. They are mineralized and contain cassiterite, molybdenite, beryl, fluorite and secondary malachite (Abdel Naby et al., 2000).

3. Petrography

Petrographic observations of HAGI samples confirm the field-based division of the intrusion into pink granite, muscovite granite, and albite granite types. Petrographic descriptions are given below for these three types from the HAGI as well as associated greisens, pegmatites, granodiorite xenoliths in the HAGI, and the metasedimentary and granodiorite country rocks.

Pink granite consists essentially of K-feldspars, quartz, and plagioclase with minor biotite and abundant zinnwaldite (strictly, siderophyllite-polylithionite solid solution; see mineral chemistry section below). Accessory minerals are frequently abundant; they include zircon, apatite, fluorite, topaz, beryl, epidote, cassiterite, allanite, ilmenite, and Nb-Ta oxides. Anhedral to subhedral coarse crystals of K-feldspar (40-50 vol.%) —including orthoclase, perthite, and microcline — contain numerous plagioclase inclusions. Medium, euhedral to subhedral tabular crystals of plagioclase (15-25%) show sericitized cores and fresh albite rims. Quartz (25-35%) occurs as anhedral coarse crystals showing wavy extinction and as undeformed fine interstitial aggregates. There are sparse graphic intergrowths of quartz and K-feldspars. Many quartz crystals have inclusions of plagioclase, K-feldspars and zircon **(Fig. 3a)**. Biotite occurs as subhedral tabular crystals, pleochroic from pale yellow to reddish-brown, and as tiny inclusions within large K-feldspar crystals. Biotite is slightly altered into chlorite and opaques, especially along crystal margins. Zinnwaldite occurs as large, subhedral, primary magmatic crystals. Fine aggregates of secondary muscovite are also present. Nb-Ta oxides, principally columbite, occur as anhedral, subhedral, or euhedral prismatic crystals; no variations in color are apparent under the microscope. Columbite may be found included in albite **(Fig. 3b)** or biotite **(Fig. 3c)** or disseminated among other minerals **(Fig. 3d)**. The mineral names in the backscatter images (Fig. 3c, d, e) are based on microprobe and SEM analyses.

Muscovite granite is equigranular and the essential mineral constituents are K-feldspar (40-50%), quartz (25-35%), and plagioclase (10-20%) with ~5% biotite and muscovite. Accessory minerals include Fe-Ti oxides, zircon, garnet, fluorite, topaz, apatite, and Nb-Ta oxides. Secondary

minerals include sericite and chlorite. Subhedral to anhedral K-feldspar (mostly cross-hatched microcline with minor orthoclase and perthite) is occasionally kaolinitized along fracture planes. Large K-feldspar crystals may contain small anhedral inclusions of albite and quartz. Subhedral tabular plagioclase is corroded by quartz and variably altered to sericite and secondary muscovite. Quartz forms anhedral coarse crystals exhibiting wavy extinction as well as intergrowths with K-feldspars. Muscovite occurs as large subhedral crystals and as fine aggregates replacing biotite and feldspar. Some large crystals of muscovite are slightly altered at the margins to secondary muscovite, chlorite, and opaques **(Fig. 3e)**. Minor biotite occurs as subhedral tabular pleochroic crystals (reddish-brown to pale yellow), slightly altered to iron oxides and chlorite. Euhedral to anhedral crystals of garnet show high relief, crackly appearance **(Fig. 3f)**, and occasional quartz inclusions. Topaz occurs as medium subhedral crystals with moderate relief and perfect cleavage **(Fig. 3g)**. Scarce subhedral to anhedral corroded crystals of Nb-Ta oxides are observed in the muscovite granite.

Albite granite is fine-grained and white, with inequigranular to seriate or sometimes porphyritic texture. It consists essentially of quartz (25-30%), plagioclase (40-55%), and K-feldspars (20-25%). The accessory minerals include Fe-Ti oxides, muscovite, fluorite, titanite, zircon, and Nb-Ta oxides, while secondary minerals include epidote, birnessite, and sericite. Albite is the most abundant constituent of the rock, forming euhedral to subhedral fine to medium prismatic crystals and inclusions in quartz and K-feldspars. K-feldspars are less common, as anhedral to subhedral crystals with perthitic texture. Some secondary albite pseudomorphs after microcline are recognizable by their original crystal habit. Quartz occurs as anhedral to sub-rounded large crystals or as fine interstitial aggregates. Columbite is the most common Ta-Nb oxide, occurring in various forms associated with biotite **(Fig. 3h)** or interstitial to feldspar crystals **(Fig. 3i)**. The anhedral to subhedral tabular columbite crystals exhibit color variation suggestive of compositional zoning, confirmed by backscatter images and microprobe analyses. Columbite is altered along its margins into fluorcalciomicrolite and rhodochrosite.

Greisen is a light-colored alteration product composed mainly of quartz, altered feldspars, zinnwaldite, cassiterite, fluorite and highly altered mafic minerals. Some greisens are mineralized and contain visible cassiterite in considerable amounts, while others are barren. Some fluorite and quartz veins cut the greisen in outcrop. Quartz occurs as ground and fractured crystals, arranged in

lines to form veins. Feldspars are completely altered to sericite, arranged in fine segregations that define a rough schistosity. Zinnwaldite forms large subhedral fractured crystals, partly altered to chlorite. Fluorite occurs as disseminated crystals and as small veins. Large pleochroic crystals of cassiterite show obvious oscillatory zoning in the intensity of brown coloration **(Fig. 3j)**.

Pegmatite occurs as pockets or veins that cut across the margins of the pluton and extend into the country rocks. The coarse-grained hypidiomorphic texture of pegmatite is composed essentially of feldspars, quartz, and muscovite. Quartz occurs as anhedral fractured crystals and as inclusions in muscovite. Interstitial muscovite is fractured and partly altered to chlorite. Fluorite occurs as small veins that include fine garnet crystals and as subhedral and anhedral interstitial crystals.

G**ranitoid xenoliths** are observed only in the muscovite granite. They are medium-grained rocks with hypidiomorphic texture, composed of quartz, plagioclase, K-feldspars and mafic minerals. Fe-Ti oxides, titanite, and zircon are found as accessory minerals. Euhedral to subhedral tabular crystals of plagioclase are the main constituent. Some plagioclase crystals are zoned and exhibit Carlsbad twinning. Anhedral to subhedral crystals of K-feldspars show perthitic texture and microcline tartan twinning. Anhedral crystals of quartz show wavy extinction. Mafic minerals include biotite with minor amphibole. The anhedral corroded crystals of biotite are pleochroic from brown to pale green and highly altered to chlorite and iron oxides. Amphibole occurs as fine green flakes, slightly altered to iron oxides.

In outcrop, all the contacts of the HAGI are with metasedimentary rocks, but the presence of xenoliths of granodiorite imply contact between the HAGI and the nearby granodiorite-tonalite unit in subcrop. The gneissose **metasedimentary country rocks** are composed mainly of plagioclase, quartz, biotite, and hornblende. Coarse anhedral crystals of plagioclase with albite twinning are often slightly altered and may enclose quartz crystals. Fine to medium grained biotite is green to brown in color, segregated into gneissic foliation bands, and stained by opaques.

Granodiorite is medium- to coarse-grained with hypidiomorphic granular to gneissose texture. A few exposures of the granodiorite exhibit porphyritic texture. It is composed of plagioclase, quartz, K-feldspar, and mafic minerals. Apatite, zircon, allanite, titanite, and Fe-Ti oxides are the most common accessory minerals. Plagioclase (35-50%) is the dominant mineral and occurs as subhedral to anhedral fresh twinned crystals. It shows variable degrees of

saussuritization and some crystals are zoned. The K-feldspars (25-35%) occur as coarse anhedral crystals of orthoclase perthite, interstitial to plagioclase. Quartz (25-35%) is not uniform in amount or distribution. It occurs mainly as anhedral crystals and as fine interstitial aggregates. The mafic minerals include biotite with minor hornblende. Biotite occurs as subhedral tabular crystals that may include zircon or apatite and as fine aggregates. Some biotite is extensively altered to chlorite, decorated by iron oxides along cleavage planes. Hornblende occurs as anhedral, strongly pleochroic, short prisms.

Tonalite is less common than granodiorite; its mineralogy is similar but tonalite has a higher fraction of mafic minerals and less quartz and K-feldspars than granodiorite. Tonalite is coarse-grained with hypidiomorphoric texture and composed essentially of plagioclase (50-60 %), quartz (20-25%), K-feldspars (<10%), biotite, and amphibole. Accessory minerals include opaques, zircon, apatite, and titanite. Plagioclase is the main feldspar and occurs as subhedral to anhedral tabular crystals. The large crystals of plagioclase show normal zoning; others are variably altered to sericite in the cores. K-feldspar occurs as anhedral fine interstitial crystals. Quartz usually forms anhedral interstitial crystals that often display undulose extinction. Subhedral tabular crystals and fine interstitial flakes of biotite and anhedral, short prismatic crystals of amphibole are both slightly altered to chlorite and opaques.

4. Analytical techniques

Representative samples of Homrit Akarem granites, granodiorite from the country rock, and granodiorite xenoliths within the HAGI were analyzed for major, trace and rare earth elements. Mineral chemical analyses and mineral identifications, backscattered electron images, and X-ray maps were obtained for selected HAGI samples. Zinnwaldite was additionally analyzed for Fe^{3+}/Fe^{T} and Li content. Full analytical methods are described in the *Supplementary Material*.

5. Mineral chemistry

Electron microprobe analyses were carried out on key minerals (feldspars, micas, Nb-Ta oxides, garnet, zircon and birnessite) in representative samples of the Homrit Akarem intrusion. Zinnwaldite in pink granite was further characterized by Mössbauer spectroscopy to define its Fe^{3+} content and by laser-ablation inductively-coupled plasma mass spectrometry (LA-ICP-MS) to

determine its Li content. All electron microprobe and LA-ICP-MS data are given in the supplementary tables (1S-10S). Additional analyses by scanning electron microscope energy-dispersive X-ray spectroscopy (SEM/EDS) helped to confirm the identification and constrain the composition of accessory phases including birnessite, thorite, zircon, xenotime-(Yb), columbite, fluorcalciomicrolite, cassiterite, fluocerite, bastnaesite-(Ce), parasite-(Nd), florencite-(Ce), and native tin. Mineral compositions by EDS are given in supplementary table 11S and corresponding backscattered electron images of key accessory phases are given in supplementary figures S1 and S2.

5.1. Feldspars

Feldspars were analyzed in all rock phases of the HAGI. The analyses and structural formulae (on the basis of 8 oxygen atoms) of feldspars are given in supplementary tables 1S (K-feldspar), 2S (albite) and 3S (plagioclase). K-feldspars are confirmed to be homogenous, nearly pure $KAlSi_3O_8$, with K_2O content ranging from (15.3-16.4 wt %) and Or content ranging from (95.9-99.1 mol %). Albite is the principal plagioclase mineral in all units of the HAGI. In all analyzed samples, albite is nearly pure $NaAlSi_3O_8$, with very low An content (<0.74 mol %) and high albite content (97.9-99.7 mol %). Ca-bearing plagioclase is found only in pink granite and muscovite granite; it is mainly oligoclase ($An_{11.8-24.3}$). We have not attempted to reconstruct the original composition of perthite grains, but the presence of distinct K-feldspar and albite crystals in all rock varieties of the HAGI suggests crystallization under subsolvus conditions followed by minor exsolution.

5.2. Micas

The analyzed micas include biotite, zinnwaldite, and muscovite. Biotite was analyzed only in pink granite; compositions and structural formulae (on the basis of 22 oxygen atoms) are given in supplementary table 4S. On the TiO_2-FeO-MgO ternary diagram of Nachit et al., (2005), the biotite analyses all plot in the primary magmatic field **(Fig. 4a)**. Using the biotite discrimination diagram of Abdel-Rahman (1994), all biotite analyses in the pink granite plot in the peraluminous field **(Fig. 4b)**.

Muscovite was analyzed in pink granite and muscovite granite; zinnwaldite was analyzed in albite granite. Supplementary table 5S presents compositions and structural formulae (on the basis of 24 oxygen plus fluorine atoms and assuming 4 F+OH per formula unit) for primary and secondary muscovite in muscovite granite and albite granite and for zinnwaldite in pink granite. The zinnwaldite in pink granite contains more fluorine than OH. It contains appreciable Zn and Mn. Refining the mineral chemistry of this sample requires knowing the oxidation states of the Fe atoms in the formula, so we collected a Mössbauer spectrum on a 100 mg split of zinnwaldite from sample HAK9. The Mössbauer spectrum (**Fig. 4c**) can be fit by two doublets (**Table 1**), consistent with single octahedral site environments for Fe^{2+} and Fe^{3+}, respectively (note, some polylithionite-siderophyllite micas have split Fe^{2+} sites, Levillain et al., 1981). The peak areas indicate Fe^{3+}/Fe^{T} = 0.407, so we have computed mineral formulae for electron microprobe analyses of zinnwaldite assuming this ratio. Electron probe totals also show a significant deficit indicating the presence of some unanalyzed element(s). Micas in similar rocks are rich in lithium, so the zinnwaldite was analyzed for Li by LA-ICP-MS. The laser spot size is much larger than the electron probe analytical volume, so individual Li analyses cannot be directly associated with individual electron probe analyses. Hence, given the absence of any obvious zoning pattern in the electron probe analyses, we used the average of four laser spots on each analyzed crystal to calculate mineral formulae for all electron probe spots in the same crystal. Li_2O contents range from 3.18 to 3.69 wt. %. The zinnwaldite analyses are plotted in the "Foster diagram", a ternary Li-R^{3+}-R^{2+} plot of octahedral site occupancy, and compared to the Pikes Peak Batholith suite of Foord et al. (1995) in **Fig. 4d**. The zinnwaldite in the HAGI pink granite closely resembles those from evolved miarolitic Nb-Y-F pegmatites from Pikes Peak as well as the zinnwaldite from the Fawwarah Fe-Li mica-bearing granitoid of the north eastern Arabian Shield (not shown; du Bray et al., 1994).

Petrographically, we observe primary muscovite only in muscovite granite and secondary muscovite in all three rock types (pink granite, muscovite granite and albite granite). Typically, primary muscovite has higher TiO_2 and lower MgO than secondary muscovite. Using the Ti-Mg-Na ternary discrimination diagram after Miller et al. (1981) **(Fig. 4e)**, the petrographically primary muscovite in muscovite granite indeed plots in the primary field, whereas the secondary muscovite in muscovite granite and albite granite plots in the secondary field. Zinnwaldite in pink granite is

not plotted because it is unknown whether this discrimination diagram can be applied to this material; however the texture of zinnwaldite suggests a primary origin.

5.3. Nb-Ta oxides

Nb-Ta oxides analyzed by electron microprobe are limited to columbite and fluorcalciomicrolite. Columbite is the main primary Nb-Ta bearing phase in all lithologic subtypes of the HAGI, while fluorcalciomicrolite is the main secondary phase. High-magnification SEM imaging reveals Ta-rich outer rims on some columbite grains, too small to be analyzed by electron probe. The chemical analyses and structural formulae of columbite and fluorcalciomicrolite are given in supplementary tables 6S and 7S (in addition, SEM/EDS analysis of narrow Ta-rich rims on columbite are given in supplementary table 11S). All the analyzed columbite crystals are dominated by Nb_2O_5, Ta_2O_5, MnO, and FeO; the only other oxide detected is TiO_2. Columbite has Ta/(Nb+Ta) ratios 0.06-0.42 and Mn/(Mn+Fe) ratios from 0.49-1; hence essentially all analyzed points are classified as columbite-(Mn) **(Fig. 4f)**. Columbite in the albite granite is notably richer in Mn and Ta than that in pink granite.

Fluorcalciomicrolite is observed only in the albite granite unit. It forms well-defined overgrowth or replacement mantles around primary columbite, separated by sharp boundaries. The major oxides are Ta_2O_5, CaO, and Nb_2O_5, with smaller but significant amounts of Na_2O. SiO_2 is not reported because the interference of Ta $M\alpha_1$ X-rays on Si $K\alpha$ is too severe for confident detection of Si in this mineral. TiO_2 concentrations are low and other oxides (FeO, MnO, MgO) are detected only sporadically. Fluorine was not quantitatively analyzed on the electron microprobe, but it is evident in energy dispersive X-ray spectra taken by SEM on this mineral, with EDS-based concentration estimates sufficient to assign the name fluorcalciomicrolite to this material (supplementary table S11).

5.4. Garnet

Garnet was observed and analyzed only in the muscovite granite; compositions, structural formulae on a 12 oxygen basis, and end-member fractions are given in supplementary table 8S. Fe^{3+} was estimated by charge balance and stoichiometry. All the garnet analysis points are manganese rich, with 28.8-29.4 wt % MnO. The end-member proportions $Sps_{66.1\text{-}67.2}Alm_{27.9\text{-}}$

$_{29.9}Prp_{2.3\text{-}3.0}Grs_{0.5\text{-}0.7}$ indicate spessartine-almandine solid solutions; spessartine and almandine together exceed 95 mol % of every analysis. The homogeneous chemistry and subhedral to euhedral form suggest a magmatic origin for the analyzed garnets. The spessartine-rich garnet compositions in the HAGI are similar to those commonly crystallized from silicic highly-fractionated magmas at low pressure (Patiño Douce 1999; Abuamarah et al., 2021; Azer et al., 2019; Seddik et al., 2020).

5.5. Zircon

Zircon compositions were determined in pink granite and muscovite granite; compositions and calculated structural formulae are given in supplementary table 9S. Two varieties of zircon are recognized in the pink granite. Primary zircons are smaller, have few inclusions and low HfO_2 contents (1.8 to 2.1 wt.%). Secondary zircons are large (up to 300 μm), riddled with inclusions, and have extreme HfO_2 contents (8.4 to 12.8 wt. %). Secondary zircons also contain appreciable Mn, P, F, Yb, U (up to 1.9 wt.%), and often Th (up to 0.54 wt. %); the presence and concentrations of these elements is confirmed by energy-dispersive X-ray analysis by high-resolution SEM (supplementary table S11). Most of the analyzed zircons, especially the secondary zircons, yield somewhat low electron probe analytical totals (as low as 90.9 wt. %), which likely reflect the metamict character of these Neoproterozoic, highly radioactive, zircons. These mineralogical observations are consistent with the high common Pb, reverse discordance, and complex cathodoluminescence observed in zircons from the HAGI dated by Ali et al. (2012).

5.6. Birnessite

Birnessite is a hydrous Mn oxide mineral. The compositions and calculated structural formulae of birnessite crystals are given in supplementary table 10S. The analyses are dominated by MnO, with other measured oxides (FeO, CaO, and Na_2O) ≤ 3 wt.%. Analytical totals of ~70 wt. % reflect the hydrous nature of this mineral. The identification of this material as birnessite was confirmed by Raman spectroscopy. Birnessite contains blebs of an unidentified Fe-rich hydroxide material.

5.7. Additional analyses by SEM/EDS

A number of accessory minerals in the HAGI samples are too small for quantitative electron probe analysis or contain appreciable concentrations of long lists of elements that are challenging to standardize for or analyze with a limited number of microprobe spectrometers. These minerals were identified and analyzed with energy-dispersive X-ray spectroscopy on a high-resolution field-emission SEM. They include thorite (in solid solution with xenotime-(Yb)), cassiterite, Ta-rich rims on some columbite-(Mn) grains, exotic high-Hf zircons, fluocerite, bastnaesite-(Ce), parasite-(Nd), florencite-(Ce), and native tin. Backscatter images and EDS spectra of these minerals are reported in supplementary **Figures S1** and **S2**; quantified analyses are reported in supplementary table 11S.

6. Whole rock geochemistry

6.1. Geochemical characteristics

The whole-rock major element, trace element, and rare earth element data of the analyzed samples are listed respectively in **Tables 2, 3,** and **4**. Note that the whole-rock analytical methods used do not allow quantification of Li or F contents; these were only measured *in situ* in zinnwaldite. All the samples are felsic, with high SiO_2, Al_2O_3, Na_2O and K_2O contents and low TiO_2, Fe_2O_3, CaO, MgO, and MnO contents. On the multicationic R_1-R_2 classification diagram of (De la Roche et al., 1980), where $R_1 = 4Si - 11(Na+K) - 2(Fe+Ti)$ and $R_2 = 6Ca + 2Mg + Al$, all but one of the HAGI samples plot in the alkali granite field **(Fig. 5)**, whereas the country rock granodiorite and HAGI xenoliths plot in the granodiorite field. The normative mineralogy (Table 2) of all samples is dominated by quartz, orthoclase and albite, with minor amounts of anorthite, hypersthene, and corundum. Normative quartz contents are 29-35 wt % and hence notably lower than the low-pressure H_2O-saturated minimum melt composition (~40 wt % normative quartz). The major oxides of the HAGI samples show mostly smooth variations across their narrow range in silica on Harker variation diagrams: K_2O generally increases with increasing SiO_2, while Al_2O_3, MgO, CaO and Na_2O decrease with increasing SiO_2 **(Fig. 6)**. $Fe_2O_{3(t)}$ is essentially uncorrelated with SiO_2 (a critical *p*-value of 0.01 is used to assess the statistical significance of correlation on each variation diagram) while TiO_2, MnO and P_2O_5 (not shown) are at essentially negligible concentrations.

The trace element character of the HAGI samples is marked by progressive enrichment of Rb, Y, Ta, Nb, and Ga alongside depletion of Sr, Ba, Sc, V, Ni, Co, and Cr. These enrichments and depletions generally become more pronounced with increasing SiO_2 **(Fig 7)**, although some trace elements are well-correlated with SiO_2 and others are not. Elements such as Zr, Zn, Pb, U, Th, Hf, Sn and W that do not correlate with SiO_2 are not plotted in Fig. 7. The trace element trends are broadly similar to other rare-metal bearing granites in the ANS, although some intrusions extend to substantially greater enrichments of the rare metals (Azer et al., 2019; Heikal et al., 2019; Abuamarah, 2020; Seddik et al., 2020; Abuamarah et al., 2021).

Primitive mantle normalized multi-element patterns of HAGI granites, country rock granodiorite and HAGI xenolith samples are shown in **Fig. 8a** (using normalization values of Sun and McDonough, 1989). The HAGI samples display uniform patterns marked by large enrichment in some large-ion lithophile elements (LILE: Rb, K, Th) and high field strength elements (HFSE: Ta, Nb, Zr, Hf) alongside clear depletion in Ba, Sr, P and Ti. This pattern is common in A-type granites (Jahn et al., 2001; Wu et al., 2002). The extensive fractional crystallization of feldspars, apatite and Fe-Ti oxides likely create the obvious depletions in Ba, Sr, P, and Ti, respectively. The granodiorite country rocks and xenoliths within the HAGI show obviously different patterns from the granites of HAGI, indicating different sources. These samples are moderately enriched in LILE with negative anomalies in HFSE (Nb-Ta trough), Sr, P, and Ti. These are all signatures of moderately fractionated subduction-related magmas.

Chondrite-normalized REE patterns are shown in **Fig. 8b**. The HAGI granite samples have nearly parallel REE patterns with about a factor of two range in enrichment of all REEs except Eu from pink granite to albite granite. They are characterized by obvious enrichment of HREE relative to LREE [$(La/Lu)_n$ = 0.22-0.48]. All the samples exhibit strong to extreme negative Eu anomalies, [(Eu/Eu*)= 0.02-0.26]. Alongside depletions of two orders of magnitude or more in Sr and Ba, this likely reflects a protracted history of feldspar fractionation. The HAGI samples display a minor but readily apparent "M-type" REE tetrad effect, as noted by Ali et al. (2012), with the $TE_{1,3}$ parameter of Irber (1999) averaging 1.11 in pink granite, 1.08 in muscovite granite, and 1.10 in albite granite. The granodiorite country rocks and xenoliths within the HAGI show REE patterns that are obviously distinct from the HAGI granites but parallel to one another, with about a factor of three range in ΣREE. They have LREE enrichment [$(La/Lu)_n$ = 5.10-12.82], nearly flat HREE [$(Gd/Lu)_n$

=1.27-1.77], slightly negative to negligible Eu anomalies [Eu/Eu* = 0.75-1.01], and negligible or very slight "W-type" tetrad effects.

6.2. Magma type

The whole-rock chemistry of the HAGI and granodiorite country rock samples can be plotted on a variety of discrimination diagrams to characterize their magmatic type and tectonic affinity. All the HAGI granite samples and xenoliths and all but one of the granodiorite country rock samples have peraluminous character, with alumina saturation index [ASI = $Al_2O_3/(CaO+Na_2O+K_2O)$ on a molar basis] greater than unity and corundum (0.11-2.86 wt.%) in their norm (Table 2). This peraluminous character is consistent with the presence of primary muscovite in most samples, development of garnet and topaz in the muscovite granite, and the mineral composition of biotite (**Fig. 4b**). Most HAGI samples have agpaitic index values [AI = (Na+K)/Al on a molar basis] greater than 0.87 (Table 2), indicating some degree of alkaline character (Liégeois and Black, 1987; Liégeois et al., 1998), whereas the granodiorite country rock and xenolith samples have AI ≤ 0.65, indicating subalkaline affinity. The discrimination diagram of Sylvester (1989) **(Fig. 9a)** places the granites of HAGI in the highly fractionated calc-alkaline field and the granodiorite and xenolith data in the calk-alkaline field.

The granite samples of the HAGI share all the characteristics of A-type granites, such as high Ga/Al, Nb, Zr, Y, Ta, and Th alongside significant depletion in MgO, CaO and P_2O_5 (Bonin, 2007; Eby, 1990, 1992; Whalen et al., 1987). On the Ga/Al vs. $FeO_{(t)}$/MgO and Ga/Al vs. Nb discrimination diagrams of Whalen et al. (1987), the HAGI samples display clear A-type character whereas the granodiorite country rock and xenoliths samples plot in the I-, S-, and M-type field **(Fig. 9b, c)**. The major-element discrimination diagram of Frost et al. (2001) also indicates a typical A-type signature for the HAGI and I-type character for the granodiorite and xenolith samples **(Fig. 9d)**. Although extensive fractional crystallization of I-type calc-alkaline granites can produce A-type residual liquids (e.g., Clemens et al., 1986; Whalen et al., 1987; King et al., 1997), in the present case it is evident that the HAGI is not evolved from the granodiorite or any common parent. On the Y/Nb vs. Rb/Nb diagram of Eby (1992), the granite samples of the HAGI plot in the A_2-type granite field **(Fig. 9e)**.

7. Discussion

One of the most striking features of the northernmost segment of the ANS is the abundance of post-collisional felsic plutons including rare-metal bearing granites (e.g., Helba et al., 1997; Küster, 2009; El Hadek et al., 2016; Abuamarah, 2020; Abdallah et al., 2020; Seddik et al., 2020; Abuamarah et al., 2021). Despite the economic significance of these granites, their origin and evolution are not yet well-understood and no overall regional pattern has emerged in their degree of mineralization and economic potential. Since the HAGI has all the common characteristics of the post-collisional rare-metal bearing granites of the ANS and a distinctive location at the western limit of the south Eastern Desert basement outcrop, constraints on its origin bear on the general geodynamic and geochemical model for tectonic setting, magmatic sources, petrogenetic processes, alteration, and ore-formation mechanisms responsible for this class of intrusions.

7.1. Tectonic setting

The chemical characteristics and intrusive field relations all require a post-collisional within-plate setting for the HAGI. It intrudes metamorphosed volcano-sedimentary sequences of the island-arc stage of ANS development and carries xenoliths of older calc-alkaline subduction-related magmas. The HAGI is not modified by regional metamorphism, only by limited brittle faulting and cataclasis. On the SiO_2-Al_2O_3 diagram of Maniar and Piccoli (1989) **(Fig. 10a),** the HAGI samples cluster within the post-orogenic granite field (POG).

Using the Nb vs. Y tectonic discrimination diagram of Pearce et al. (1984), all the HAGI samples plot well into the within-plate granite field **(Fig. 10b)** (although they plot within the upper range of anomalous ocean-ridge granites on this diagram, this is not a plausible interpretation of these rocks), whereas the granodiorite country rock and xenolith samples plot in the volcanic arc granite field. On the R_1-R_2 diagram of De La Roche et al. (1980), with tectonic setting fields based on Batchelor and Bowden (1985), the HAGI samples plot with one exception in the post-orogenic field **(Fig. 10c)** and the granodiorite samples plot in the pre-collision field (note the size of symbols on this figure is much larger than the error, based on analytical uncertainty of 1% for each major oxide). Finally, although mobility of Rb may be a concern for the use of the Rb/30 - Hf- 3*Ta ternary diagram of Harris et al. (1986), all the HAGI samples plot as expected in the within-plate field **(Fig. 10d)** and all the granodiorite and xenolith samples in the volcanic-arc field. Recalling

that the HAGI samples plot in the A2 field on the Y/Nb-Rb/Nb diagram **(Fig. 9e),** this field is considered characteristic of post-collisional rocks derived from crustal sources (Eby, 1992).

7.2. Source rocks and magmatic processes

A confusing variety of names have been assigned to rare-metal granites in the Eastern Desert, including apogranite, albitized granite, albite granite and leucogranite. Likewise, a variety of hypotheses for the origin of these rocks have been published (e.g., Helba et al. 1997; Küster 2009; El Hadek et al. 2016; Emam et al. 2018; Azer et al., 2019, 2020; Seddik et al., 2020). The large differences in major and trace elements concentrations and isotope ratios among all the post-collisional A-type granitoids of the ANS suggest that a variety of sources and processes were involved in their genesis (Abdel-Rahman, 2006; Farahat et al., 2007; Ali et al., 2016; Emam et al., 2018; Heikal et al., 2019; Seddik et al., 2020), but the rare-metal granites are a distinctive subgroup of these granitoids with considerable similarity from location to location.

The origins of A-type granitoids in general have been explained by petrogenetic models including (1) dehydration melting of tonalitic to granodioritic source rocks (Creaser et al., 1991; King et al., 1997); (2) fractional crystallization of mantle-derived basaltic magma (Haapala et al., 2007; Li et al., 2007; Wu et al., 2002); (3) partial melting of residual source rocks after the extraction of I-type magmas (Collins et al., 1982; Whalen et al., 1987); (4) low-pressure melting of calc-alkaline rocks at upper crustal levels (Patiño Douce, 1997; Skjerlie and Johnston, 1993) and (5) hybridization of mantle-derived magmas with crustal melts (Yang et al., 2006).

The literature on the late Neoproterozoic rocks of the Homrit Akarem area, studied by a number of authors (e.g., Hassanen et al., 1995; Hassanen and Harraz, 1996; Abd El-Naby et al., 2000; Mohamed et al., 2009; Ali et al., 2012), includes conclusions spanning nearly the entire range of models for A-type magmatism. According to Hassanen and Harraz (1996), the HAGI is a post-collisional granite derived from mixing of mantle-derived magma with variable amounts of crustal components, followed by albitization of the upper part of the pluton due to post-magmatic hydrothermal metasomatism. Abd El Naby et al. (2000), by contrast, concluded that the HAGI formed during the collisional stage by anatexis of the island-arc stage metasedimentary series. Mohamed et al. (2009) assumed that the HAGI is a typical post-collisional A-type granite and focused on the role of post-magmatic F-rich fluid in causing albitization and greisenization around

510 the pluton. Ali et al. (2012) proposed that the HAGI evolved from highly fractionated magma and
511 differed from Mohamed et al. (2009) in arguing that the greisenization, albitization, and enrichment
512 in HFSE and HREE reflect the action of late-stage magmatic (as opposed to post-magmatic) F-rich
513 fluids. Ali et al. (2012) offered two interpretations of their U–Pb SHRIMP zircon ages from the
514 HAGI and the nearby Homrat Mukbid intrusion: either magmatic emplacement at 630-620 Ma and
515 disturbance by fluid interaction at ~600 Ma (which is inconsistent with the assignment of the fluid
516 interaction as late-stage magmetic), or intrusion at ~600 Ma with incorporation of many zircons
517 from the ~630 Ma granodiorite country rock. Although Ali et al. (2012) preferred the former
518 interpretation, we note that 620-630 Ma is older than the main post-collisional activity in the
519 northern ANS. We suggest that the zircons analyzed by Ali et al. (2012) that crystallized from the
520 HAGI itself, like most of the zircons we characterized petrographically and geochemically, are
521 highly radioactive, at least partially metamict, and not suitable for high-precision U-Pb
522 geochronology. Hence we find the alternative interpretation offered by Ali et al. (2012), with
523 intrusion at ~600 Ma and F-rich fluid interaction nearly synchronous with intrusion (rather than
524 >20 Myr later) to be most consistent with the full range of available data.
525 We find no support in our data for the collisional-stage hypothesis of Abd El Naby et al.
526 (2000). All indicators point to a post-collisional setting for intrusion of the HAGI in the final stage
527 of ANS evolution. The HAGI is marked by sharp, distinct intrusive contacts against the
528 metasedimentary country rocks with a thin contact metamorphic aureole indicating high-
529 temperature, low-pressure interaction; no anatexis of the country rock is apparent at current outcrop
530 level. On the other hand, the whole unit defined here as the HAGI is clearly co-genetic. Within the
531 discrete masses of the HAGI there are both gradational and sharp boundaries among the petrologic
532 types. The trace element and REE patterns of the different rock types are all similar and smoothly
533 varying, and there are no compositional gaps in major or trace element concentrations **(Figs. 6 and**
534 **7)**. Additional evidence for derivation of all the HAGI rocks from a common source evolving by
535 fractional crystallization comes from continuous and coherent evolutionary trends of compatible
536 and incompatible elements and their ratios (**Fig. 11**).
537 The absence of mafic and intermediate igneous rocks, enclaves, or mafic xenocrysts in the
538 HAGI argues against derivation from a mantle-derived mafic magma. Instead, the available
539 geochemical data for the HAGI indicate their generation through partial melting of a juvenile

crustal source, followed by extensive fractional crystallization and probable upper-crustal contamination (recorded by granodiorite xenoliths and perhaps by inherited zircons from the granodiorite). In general, crustal sources have elevated Nb/Ta ratios compared to those of mantle sources (Smirnov et al., 1983). The studied granites have higher contents of Nb (39-59 μg/g) than Ta (11-29 μg/g), expressed by a mineralogical predominance of columbite and absence of tantalite. Although Nb/Ta is elevated in crustal sources, Rb and Y are even more enriched than Nb, leading Eby (1992) to define the A_2-type granite field on the Y/Nb vs. Rb/Nb diagram **(Fig. 8e)** and associate it with magmas derived mainly from continental crust. As noted above, the HAGI is an A_2-type intrusion.

Every granite sample of the HAGI is peraluminous, with ASI > 1.0 and corundum in the norm. Experimental results indicate that melting of metasedimentary schists and gneisses, whose protoliths were pelitic sediments or quartz-rich aluminous greywackes, would yield peraluminous melts (Montel and Vielzeuf, 1997). This is not a unique interpretation, however. The results of Patiño Douce (1997) indicate that dehydration melting of calc-alkaline tonalite at 950°C and 0.4 GPa can also produce peraluminous melts with the major and trace element characteristics of A-type magmas. In either case, though, suitable source rocks whose partial melting might yield the parental magma of the HAGI are available among the Neoproterozoic crustal rocks of the ANS. The presence of granodiorite xenoliths in the HAGI suggests some role for assimilation of wall rock into the intrusion. This is supported by the presence of older zircons (740-703 Ma and arguably ~630 Ma as well) (Ali et al., 2012), likely inherited from older granitoids in the region. The granodiorite in the study area represents an older generation of subduction-related magmatism and is not co-genetic with post-collisional HAGI.

The geochemical characteristics of the HAGI indicate its evolution as a single magmatic suite from a common parental magma by extensive fractional crystallization and fluid modification. The good correlations between SiO_2 and most major and trace element concentrations **(Figs. 5 and 6)** are consistent with fractional crystallization in the evolution of the two suites. This is supported by the observation that samples of all three rock types form single trends in Rb/Sr vs. Sr**,** Rb/Ba vs. Rb/Sr, Rb vs. K/Rb and Nb vs. Ta plots **(Fig. 10a-d)**. The parallel primitive mantle-normalized spider diagrams **(Fig. 7a)** and REE patterns **(Fig. 7b)** also reflect common parentage and progressive magmatic evolution through the suite. Negative anomalies in Eu, Sr, and Ba are

attributed to feldspar fractionation, whereas negative P and Ti anomalies more likely reflect fractionation of apatite and Fe-Ti oxides. The granites of HAGI show wide variations in Zr/Hf ratios (20-62), indicating extreme magmatic fractionation and fluid interaction (Ballouard et al., 2016). Enrichment in Nb sufficient to form columbite is also an indicator of extensive concentration by fractionation crystallization (Wang et al., 2017), whereas secondary minerals rich in Ta likely reflect redistribution of rare metals by fluids.

7.3 Comparing the Homrit Akarem granite with related intrusions in the ANS

The HAGI is located near the western limit of the south Eastern Desert basement exposure, ~50 km west of the nearest related intrusion, at Nikeiba. Together, the El-Gharabiya, Nikeiba, and Homrit Akarem intrusions constitute a transect across the south Eastern Desert and therefore the HAGI data for the first time allow a geochemical assessment of whether trends in rare-metal granite chemistry across the south Eastern Desert basement exposure are similar to or different from the better-known trend defined by the 10 rare metal granites exposed across the central Eastern Desert (the very isolated Um Ara intrusion farther to the South is difficult to place in regional context).

The mode of emplacement of the HAGI is very similar to the other ANS post-tectonic rare-metal bearing granites (e.g., Azer et al., 2019, 2020; Seddik et al., 2020; Abuamarah et al., 2021a, b), but the chemical compositions of these intrusions are quite distinct. The HAGI represents a magmatic cupola at the very top of a post-collisional intrusion, much like the Abu Dabbab and Mueilha intrusions of the Eastern Desert (Seddik et al., 2020; Abuamarah et al., 2021a). However, the Abu Dabbab intrusion is highly mineralized and contains much higher concentration of niobium and tantalum than the HAGI and Mueilha intrusions. The HAGI is also similar to the Ad-Dayheen granite intrusion of the Arabian Shield, but the latter and its associated pegmatites are again highly mineralized and contain higher concentrations of U, Th, Zr, Nb, Ta, Y, Hf and ∑REE than the HAGI (Moghazi et al., 2011; Abuamarah et al., 2021b).

Hence, our HAGI results can be interpreted as evidence of a pattern useful for prospecting and resource evaluation: the largest enrichments in rare metals and highest ore potential occur in granites exposed in the eastern half of the Nubian Shield or across the Red Sea in the Central Arabian Shield. The decline in resource potential towards the western limit of the Nubian Shield applies to the south Eastern Desert transect as well as the central Eastern Desert transect. Indeed,

preliminary studies of the Nikeiba intrusion show Nb concentrations 100-456 μg/g (Eliwa et al., 2018; Khaleal et al., 2007), or up to 8 times the highest Nb enrichment found at Homrit Akarem. This pattern suggests that resource evaluation of the essentially unstudied El-Gharabiya intrusion, at the eastern end of the south Eastern Desert transect, is a high priority.

There are also rare-metal granites ringing the eastern limit of exposure of the Arabian Shield (du Bray et al., 1994), which feature in some cases zinnwaldite similar to that reported here in the HAGI. It may prove fruitful to extend the principle of regional patterns of mineralization potential from the western limb of the Nubian Shield to the eastern limb of the Arabian Shield.

7.4 Potential of Fe^{3+}-rich, F-rich zinnwaldite for assessment of magmatic intensive parameters

Zinnwaldite in pink granite contains notable concentrations of F, Fe^{3+}, Li, Mn, and Zn. The concentrations of these elements have been tracked through the stages of magmatic evolution in well-exposed anorogenic batholiths such as at Pikes Peak, Colorado, USA (Foord et al., 1995; Kile and Foord, 1998). The Zinnwaldite at Homrit Akarem most closely matches that found in miarolitic cavities within Nb-Y-F granitic pegmatite phase of the Pikes Peak suite, which were assigned by Kile and Foord (1998) to the last stages of magmatic crystallization. It is notable that Fe-Li micas found distributed within the mass of rare-metal plutons in the ANS (this work, du Bray et al., 1994) are most similar to those found in highly evolved pegmatite veins elsewhere (Foord et al., 1995). This observation and the primary texture of zinnwaldite in the pink granite of the HAGI support the assignment of this phase to a magmatic origin but also confirms that the current exposure of the HAGI represents a magmatic cupola. The cupola atop a pluton is an accumulation zone for late-magmatic, highly-evolved fluids that are poised, under suitable rheologic conditions, to be injected as miarolitic pegmatites. In the ANS plutonic cupolas, this material crystallized in place as well as forming pegmatites and greisen.

Some experimental calibration is available to aid interpretation of zinnwaldite composition as a geochemical indicator. It has the potential to define the oxidation state and F/OH activity ratio of its parental melt, and hence to resolve the rare-metal transporting complexes and the ambiguity between pressure and F content as factors driving the bulk compositions of rare metal granites towards low normative quartz contents.

The classic experimental work of Manning (1981) on the effect of magmatic F on phase equilibria in the quartz-albite-orthoclase system at 0.1 GPa revealed that increasing F activity

causes a shift in the location of the minimum on the quartz-alkali feldspar cotectic towards lower normative quartz and slightly higher Ab/Or ratio (**Figure 12**). The trend due to F enrichment is similar to the effect of increasing pressure in the F-free H_2O-saturated system, which also lowers normative quartz alongside a stronger increase in the Ab/Or ratio. The addition of 4 wt % F induces an effect on the normative quartz content of the minimum melt comparable to an increase to ~0.9 GPa pressure. Although the pressure-driven and F-driven traces of the minimum melt composition are different in terms of Ab/Or ratio, this is a very challenging diagnostic to use in the assessment of emplacement conditions for A-type granites because their alkali contents are inevitably modified by late-magmatic or post-magmatic fluid-driven metasomatism. Hence there is an ambiguity of interpretation, unless independent means are available to fix the pressure of fractional crystallization that ultimately controls the major element composition of a given pluton.

In this context, the discovery of F-rich zinnwaldite in rare-metal granites in Egypt is highly significant. A study of the miscibility gap between dioctahedral and trioctahedral micas by Monier and Robert (2018) suggests that crystallization of a single zinnwaldite composition instead of a biotite-like and a muscovite-like immiscible pair requires F/Li > 1. Experimental work by Munoz and Ludington (1977) established an equilibrium constant for OH-F exchange between muscovite and fluid. This work showed that muscovite typically incorporates much less F than trioctahedral micas such as phlogopite, annite, or siderophyllite when equilibrated with the same F/OH fluid activity buffer (anorthite-fluorite-sillimanite-quartz, AFSQ). Indeed, at 0.2 GPa and the AFSQ buffer, the highest F/(F+OH) ratio observed experimentally in muscovite is 0.31 at 690 °C. Yet the zinnwaldite in the HAGI yields F/(F+OH) averaging 0.76 and extending as high as 0.89. Naively, if the equilibrium constant for muscovite-fluid F/OH exchange of Munoz and Ludington (1977) applies to zinnwaldite, an increase in F/(F+OH) from 0.31 to 0.76 indicates an increase in the ratio of f_{H2O}/f_{HF} by ~0.9 log units above the AFSQ buffer. The provisional conclusion of this exercise is that, pending experimental calibration of the F/OH exchange equilibrium for micas more similar to zinnwaldite, the measurement of F/(F+OH) in primary magmatic mica constrains the F/OH ratio of the fluid and therefore yields an independent constraint on the pressure needed to match the normative quartz content of the F-bearing, fluid-saturated granite minimum to the normative quartz content of a given intrusion.

660 The zinnwaldite in the HAGI is also notable for its elevated Fe^{3+} content, with Mössbauer
661 spectroscopy showing $Fe^{3+}/Fe^{T} = 0.407$. Quantitative oxygen fugacity measurements for granitoid
662 magmas are challenging to obtain. Granites typically lack the mineral assemblages needed to apply
663 oxybarometers such as ilmenite-magnetite, olivine-orthopyroxene-spinel, biotite-garnet-
664 muscovite-magnetite-quartz. Their whole-rock Fe^{3+}/Fe^{2+} is rarely pristine. Ce anomalies in zircon
665 offer one avenue to estimating magmatic redox, but in Proterozoic rare-metal granites the zircons
666 may all be too radiation-damaged for this approach. Quantitative Mössbauer analysis of
667 zinnwaldite may be the best solution; preliminary calibration by Černý and Burt (1984), for
668 example, used this approach to confirm that anorogenic Nb-Y-F type pegmatites are typically more
669 oxidized than S-type Li-Cs-Ta type pegmatites. Experimental data to support a quantitative
670 estimate of oxygen fugacity from Fe^{3+}/Fe^{2+} of zinnwaldite is not presently available, but
671 qualitatively we note that the observed value is much higher, for example, than the highest value
672 observed ($Fe^{3+}/Fe^{T} = 0.16$) in late greisen associated with the W-bearing Xihuashan rare-metal
673 granite in South China (Li et al., 2021).
674
675 ***7.5. Tectono-magmatic evolution model***
676 An episode of lithospheric delamination is commonly invoked to explain the voluminous
677 post-collisional magmatism (610-590 Ma) in the ANS (e.g., Avigad and Gvirtzman, 2009; Farahat
678 and Azer, 2011; Be'eri-Shlevin et al., 2011; Obeid and Azer, 2015; Khalil et al., 2015, 2018;
679 Gahlan et al., 2018). The occurrence of dike swarms, shear zones, core complexes and strike-slip
680 faults cutting the Eastern Desert basement suggests some lithospheric extension during the post-
681 collisional stage in the north ANS (Blasband et al., 2000; Avigad and Gvirtzman, 2009). These
682 extensional structures may support transmission of anomalous heat flow to the middle crust and
683 unroofing-driven decompression, enhancing partial melting of supracrustal sequences and
684 formation of peraluminous A-type granites.
685 The proposed model for the tectono-magmatic evolution of the HAGI by partial melting of
686 the juvenile crust of the ANS during the post-collisional phase is shown in **Fig. 13**. In this model,
687 crustal and lithospheric thickening during the collision was followed by slab break-off and
688 lithospheric delamination. Delamination forces upwelling of hot asthenosphere, which results in
689 broad crustal doming and uplift of the overlying crust. Uplift is followed by rapid erosion, which

690 exhumes and decompresses the lower and middle crust. At the same time, the underplated basic
691 magma releases latent and sensible heat that is transported upwards. The potent combination of
692 decompression and temperature increase is capable of supporting substantial partial melting of the
693 lower crust, leading to a flare-up of post-collisional calc-alkaline magmatism. Storage and
694 fractionation of these crustal melts in the middle crust allow the evolution of highly fractionated
695 A-type granites. The abundance of strike-slip faults, dike swarms, and shear zones during the post-
696 collisional stage promotes the ascent of these magmas to the shallow crust, explaining their
697 common alignment along structural trends.
698 The HAGI represents a magmatic cupola above highly fractionated A-type magma.
699 Although quartz-feldspar barometry results (e.g., Gualda and Ghiorso, 2014) normally suggest
700 elevated pressure in order to move the granite minimum composition to the relatively low
701 normative quartz contents observed in the HAGI and other related A-type rare-metal granites, we
702 have clearly shown here that it is the effect of F on the phase relations, and not elevated pressure,
703 that are responsible for this feature. The present study shows that the albite granite, emplaced at a
704 shallow level, likely represents the early-crystallized portion of the intrusion at the apex of the
705 magmatic system, while the main portion of the intrusion was emplaced beneath the apex and
706 crystallized more slowly. As the main mass of HAGI pink granite crystallized, the residual melt
707 was enriched in alkalis, silica, water, fluorine, and rare metals. These fluids initially interacted with
708 the muscovite granite and albite granite phases before their complete crystallization, yielding
709 gradational contacts and primary magmatic textures in both marginal phases. However, continuing
710 escape of late melts and fluids from depth after final crystallization formed fractures that extended
711 into the country rocks and resulted in greisen, pegmatites and quartz-fluorite veins (e.g., McCarthy
712 and Fripp, 1980; Schimtz and Burt, 1990).
713
714 **7.6. Evidence of magmatic vs. metasomatic effects**
715 The rare-metal bearing granites in the Eastern Desert of Egypt have been attributed by many
716 authors to post-magmatic high-temperature metasomatic origins (e.g., Sabet et al., 1976; El-Tabal,
717 1979; Riad, 1979; Kamel and El Tabbal, 1980; El-Galy et al.,2016), while others have preferred
718 magmatic origins (e.g., Asran, 1985; Morsey and Mohamed, 1992; Jahn, 1996; Helba et al., 1997;
719 Arslan et al., 1997; Renno, 1997; Abou El Maaty and Ali Bik, 2000) or hybrid models that note

720 significant roles for both magmatic and post-magmatic processes (Azer et al., 2019; Heikal et al.,
721 2019; Seddik et al., 2020; Zoheir et al., 2020; Abuamarah et al., 2021).

722 Numerous lines of evidence support and confirm the magmatic origin of the HAGI and
723 document the preservation of important magmatic signatures despite the action of later
724 metasomatic processes. These magmatic observations include (1) sharp intrusive contacts with the
725 country rocks; (2) coherent and continuous compositional trends in major, trace, and rare earth
726 element concentrations; (3) coexistence of euhedral to subhedral crystals of primary feldspars,
727 biotite and muscovite; (4) overall enrichment in fluid-immobile rare elements, as Nb and Ta; (5)
728 well-developed columbite crystals with normal zoning; and (6) fluorite crystallizing as anhedral to
729 subhedral grains between the constituent minerals.

730 Although the dominance of magmatic features in the HAGI leads us to conclude that the
731 majority of its evolution was magmatic, the effects of later hydrothermal fluids are evident as well.
732 There is extensive replacement by secondary minerals, especially in the apical part of the intrusion
733 (albite granite) and the marginal zone (muscovite granite). We consider the parts of the intrusion
734 recording most clearly the effects of hydrothermal fluids to have crystallized earlier than the central
735 pink granite and therefore to have been more extensively modified by fluids escaping from the later
736 crystallizing magmatic core of the intrusion. Metasomatic features include: (1) development of
737 pegmatites, greisens and quartz-fluorite veins in fracture systems extending from the marginal
738 zones of the intrusion into the country rocks; (2) partial replacement of microcline by secondary
739 albite with preservation of the original crystal habit; (3) overgrowth of secondary albite around
740 primary feldspars and quartz; (4) partial alteration of albite crystals to sericite and muscovite; (5)
741 presence of biotite relics within secondary muscovite; and (6) overgrowth or replacement of
742 primary columbite by secondary fluorcalciomicrolite and rhodochrosite.

743 The presence of pegmatite veins cutting the HAGI and its host rocks indicates that the
744 granitic melt was fluid-saturated, at least in its final evolutionary stages (London, 2015; Wu et al.,
745 2020). Indeed, volatile concentrations are the key to constraining the fractionation behavior of the
746 granitic rocks of the HAGI. Pegmatite pockets display gradational contacts with the host granite,
747 suggesting that they represent products of *in situ* fractionation of granitic magma. The occurrence
748 of F-bearing minerals such as magmatic fluorite, F-rich zinnwaldite, and the alteration of Nb-Ta
749 oxide to fluorcalciomicrolite all indicate the enrichment of the magma with appreciable fluorine.

In general, F-rich fluids in granitoid systems have been assigned various to primary magmatic (e.g., Cuney et al., 1992; Dostal and Chatterjee, 1995; Agangiet al., 2010) and secondary metasomatic sources (e.g., Higgins et al., 1985; Nurmi and Haapala, 1986). In the HAGI, however, it is evident that F was present in the magma already in the magmatic stage. As emphasized above, experimental calibration of the equilibrium constant (or verification that the calibration of Munoz and Lundington, 1977, is applicable) for zinnwaldite/fluid F-OH partitioning offers a pathway to quantifying this conclusion.

Hydrothermal alteration continued into the sub-solidus in the marginal zones of the HAGI, as indicated by re-equilibration textures and formation of secondary minerals after K-feldspar, mica, and columbite. Nevertheless, a magmatic origin for the hydrothermal solutions that affected these granites is favored by the following observations: (1) fluorite forms anhedral to subhedral grains among the rock-forming minerals; (2) Nb, U, and Th concentrations are elevated and increase with extensive fractionation from the early phase (albite granite) to the late phase (pink granite); (3) the transition from the pink granites to the white albite is gradational and associated with pegmatites with gradational boundaries, pointing to crystallization of the pink granite as the source of fluids that ascended and altered the albite granite.

The presence of garnet as an accessory mineral in the muscovite granite phase of the HAGI is important in tracing the evolution of these rocks (Gaspar et al., 2008). The texture and chemical composition of garnet can be used to indicate pressure-temperature-fluid activity conditions during its growth (du Bray, 1988; Whitworth, 1992; Villaros et al., 2009; Zhang et al., 2012; Bekele and Sen, 2020). Spessartine-almandine garnets in general have many possible origins: (1) they may crystallize directly form Mn-rich peraluminous magma under suitable temperature and pressure conditions (du Bray, 1988; Dahlquist et al., 2007; Yang et al., 2013; Sami et al., 2020); (2) they may crystallize as phenocrysts in primary magma at deeper levels and be transported to higher crustal levels and emplaced (Harangi et al., 2001); (3) they may be a residual phase during partial melting (René and Stelling, 2007); (4) they may form as a secondary metasomatic phase upon interaction between post-magmatic hydrothermal fluids and host rocks (Clarke and Rottura, 1994; Kontak and Corey, 1988); and (5) they may be xenocrysts derived from partially assimilated disaggregated wall rock (Erdmann et al., 2009, Taylor and Stevens, 2010; Dorais and Tubrett, 2012). In the HAGI, accessory garnet is found only in the marginal zone that also contains abundant

primary muscovite. Although this phase of the intrusion was modified by fluids escaping from the later crystallizing core, nevertheless the textural and compositional evidence supports growth of this garnet at magmatic conditions, above the solidus. The euhedral to subhedral form of the garnet crystals, together with the presence of quartz inclusions and absence of any metamorphic mineral inclusions, suggests a magmatic origin. All the garnet analyses are spessartine-rich, typical of garnets grown from highly-evolved, silica-rich, peraluminous magma (Whitworth, 1992). The composition of garnet in the HAGI is similar to that reported from several other post-collisional granites in the Eastern Desert of Egypt (Azer et al., 2019; Abuamarah et al., 2021).

8. Conclusions

- The Homrit Akarem granitic intrusion (HAGI) is typical of the post-collisional, mineralized A-type granites of late Neoproterozoic age in the ANS. Field relationships indicate that the HAGI has sharp intrusive contacts with metamorphic country rocks, marked by a thin contact aureole of hornfels. The HAGI consists of early marginal phases of albite granite (apical part of the pluton) and muscovite granite (lateral margins) and a later central phase of pink granite.
- The rare-metal bearing A-type granites of the Eastern Desert reveal a variety of different levels of enrichment of Nb, Ta, Zr, Y, Th, U, and REEs. The HAGI anchors the western limit of a transect of rare-metal granites across the south Eastern Desert and is notably less mineralized than intrusions farther east. The HAGI helps to define a geographic pattern or greater rare-metal enrichment towards the east, or towards the axis of the ANS.
- Texture and morphology of the ore minerals indicate that they formed in two stages: a magmatic stage coinciding with emplacement of the intrusion, followed by a hydrothermal stage. Separation of fluids from the oversaturated melt promoted segregation and emplacement of pegmatite and veins of fluorite and quartz as the magmatic stage transitioned into an early hydrothermal stage.
- The pink granite at the center of the HAGI contains (F, Fe^{3+})-rich zinnwaldite. Although its application to defining intensive parameters such as f_{H_2O}/f_{HF} and fO_2 of its parental magma requires experimental calibration, comparison to other localities is sufficient to confirm the F-rich and oxidized character of the HAGI magmatic system and to confirm the effect of fluorine on the phase equilibria of anorogenic granites.

- Each phase of the HAGI defines coherent and cogenetic geochemical signatures, they can all be related to one another by simple fractional crystallization. Late- and post-magmatic fluid–rock reactions modified the texture and composition of the early-crystallized phases of the intrusion but their magmatic features are preserved.
- The HAGI case is consistent with the general geodynamic model for post-collisional magmatism in the ANS via partial melting of juvenile crustal followed by extensive fractional crystallization and a late-magmatic fluid overprint. Formation of the parent magma was likely triggered by lithospheric delamination and subsequent delivery of hot asthenospheric material to the base of an uplifted crust. Transfer of mantle-derived fluids and heat led to partial melting of the juvenile lower crustal material and ascent of melts along strike-slip faults, shear zones, and oblique extensional structures.

9. Acknowledgments

The authors would like to extend their appreciation and gratitude to the King Saud University, Riyadh, Saudi Arabia for funding and supporting this work through Researchers Supporting Project number (RSP-2020/151). PDA's participation is supported by NSF award 1947616.

10. References

Abd El Naby, H.H., Dawood, Y.H., Saleh, G.M., 2000. Pan-African granitoid magmatism in the Gabel Homr Akarem Area, South Eastern Desert, Egypt: Geochemistry and petrogenetic implications. Chemie der Erde 60(3), 251-267.

Abdallah, S.E., Azer, M.K., El Shammari, A.S., 2020. Petrological and geochemical evolution of Ediacaran rare-metal bearing A-type granites from the Jabal Aja complex, northern Arabian Shield, Saudi Arabia. Acta Geologica Sinica 94(3), 743-762.

Abdel-Rahman, A.M., 1994. Nature of biotites from alkaline, calc-alkaline and peraluminous magmas. Journal of petrology 35, 525-541.

Abdel-Rahman, A.M., 2006. Petrogenesis of anorogenic peralkaline granitic complexes from eastern Egypt. Mineralogical Magazine 70, 27-50.

839 Abou El Maaty, M.A., Ali Bik, M.W., 2000. Petrology of alkali feldspar granites of Nuweibi and
840 Gebel El-Mueilha, central Eastern Desert, Egypt. Egyptian Journal of Geology 44, 127-
841 148.
842 Abuamarah, B.A., 2020. Genesis and petrology of postcollisional rare-metal-bearing granites in
843 the Arabian Shield: A case study of Aja ring complex, northern Saudi Arabia. The Journal
844 of Geology 128, 131–156.
845 Abuamarah, B.A., Azer, M.K., Asimow, P.D., Ghrefat, H., Mubarak, H.S., 2021a. Geochemistry
846 and Petrogenesis of late Ediacaran Rare-metal Albite Granites of the Arabian-Nubian
847 Shield. Acta Geologica Sinica (Published online: https://doi.org/10.1111/1755-
848 6724.14379).
849 Abuamarah, B.A., Azer, M.K., Asimow, P.D., Shi, Q., 2021b. Petrogenesis of the post-collisional
850 rare-metal-bearing Ad-Dayheen granite intrusion, Central Arabian Shield. Lithos 384,
851 105956.
852 Agangi, A., Kamenetsky, V.S., McPhie, J., 2010. The role of fluorine in the concentration and
853 transport of lithophile trace elements in felsic magmas: insights from the Gawler Range
854 Volcanics, South Australia. Chemical Geology 273, 314–325.
855 Ali, K.A., Azer, M.K., Gahlan, H.A., Wilde, S.A., Samuel, M.D., Stern, R.J., 2010. Age constraints
856 on the formation and emplacement of Neoproterozoic ophiolites along the Allaqi-Heiani
857 suture, South Eastern Desert of Egypt. Gondwana Research 18, 583-595.
858 Ali, K.A., Moghazi, A.K.M., Maurice, A.E., Omar, S.A., Wang, Q., Wilde, S.A., Moussa, E.M.,
859 Manton, W.I., Stern, R.J., 2012. Composition, age, and origin of the ~620 Ma Humr Akarim
860 and Humrat Mukbid A-type granites: no evidence for pre-Neoproterozoic basement in the
861 Eastern Desert, Egypt. International Journal of Earth Sciences 101(7), 1705-1722.
862 Ali, K.A., Zoheir, B.A., Stern, R.J., Andresen, A., Whitehouse, M.J., Bishara, W.W., 2016. Lu–Hf
863 and O isotopic compositions on single zircons from the North Eastern Desert of Egypt,
864 Arabian–Nubian Shield: Implications for crustal evolution. Gondwana Research 32, 181-
865 192.
866 Arslan, A.I., Helba, H.A., Khalil, S.O., Morteani, G., 1997. Bedrock geochemical prospecting and
867 ore potentiality of the rare metal-bearing granite at Nuweibi area, central Eastern Desert,

868 Egypt. The Third Conference on Geochemistry, Alexandria University, Alexandria-Egypt,
869 3-4 September 1997, pp375-387.
870 Asran, M.H.A., 1985. Geology, petrography and geochemistry of the apogranites at Nuweibi and
871 Abu Dabbab areas, Eastern Desert, Egypt. Unpubl. M.Sc. thesis, Assiut University, Egypt,
872 149 pp.
873 Avigad, D., Gvirtzman, Z., 2009. Late Neoproterozoic rise and fall of the northern Arabian–Nubian
874 shield: the role of lithospheric mantle delamination and subsequent thermal subsidence.
875 Tectonophysics 477, 217–228.
876 Azer, M.K., 2007. Tectonic significance of Late Precambrian calc-alkaline and alkaline
877 magmatism in Saint Katherine area, South Sinai, Egypt. Geologica Acta 5 (3), 255–272.
878 Azer, M.K., Abdelfadil, K.M. and Ramadan, A.A., 2019. geochemistry and petrogenesis of Late
879 Ediacaran rare-metal albite granite of the Nubian Shield: Case study of Nuweibi intrusion,
880 Eastern Desert, Egypt. The Journal of Geology 127(6), 665-689.
881 Azer, M.K., Abdelfadil, K.M., Asimow, P.D. and Khalil, A.E., 2020. Tracking the transition from
882 subduction-related to post-collisional magmatism in the north Arabian–Nubian Shield: A
883 case study from the Homrit Waggat area of the Eastern Desert of Egypt. Geological Journal
884 55, 4426–4452.
885 Azer, M.K,. Asimow, P.D., 2021. Petrogenetic Evolution of the Neoproterozoic Igneous Rocks of
886 Egypt. In The Geology of the Egyptian Nubian Shield (pp. 343-382). Springer, Cham.
887 Ballouard, C., Poujol, M., Boulvais, P., Branquet, Y., Tartèse, R., Vigneresse, J.L., 2016. Nb–Ta
888 fractionation in peraluminous granites: a marker of the magmatic-hydrothermal transition.
889 Geology 44, 231–234.
890 Barker, F., Wones, D.R., Sharp, W.N., Desborough, G.A., 1975. The Pikes Peak Batholith,
891 Colorado Front Range, and a model for the origin of the gabbro-anorthosite-syenite-
892 potassic granite suite. Precambrian Research 2, 97-160.
893 Batchelor, R.A., Bowden, P., 1985. Petrogenetic interpretation of granitoid rock series using
894 multicationic parameters. Chemical Geology 48, 43-45.
895 Be'eri-Shlevin, Y., Katzir, Y., Whitehouse M., 2009. Post-collisional tectono-magmatic evolution
896 in the northern Arabian-Nubian Shield (ANS): Time constraints from ion-probe U-Pb
897 dating of zircon. Journal of Geological Society of London 166, 71-85.

898 Be'eri-Shlevin, Y., Samuel, M.D., Azer, M.K., Rämö, O.T., Whitehouse, M.J., Moussa, H.E.,
899 2011. The late Neoproterozoic Ferani and Rutig volcano-sedimentary successions of the
900 northernmost Arabian-Nubian Shield (ANS): New insights from zircon U-Pb
901 geochronology, geochemistry and O-Nd isotope ratios. Precambrian Research 188, 21-44.
902 Bekele, B., Sen, A.K., 2020. The mineral chemistry of gahnite, garnet and columbite-group
903 minerals (CGM): Implications for genesis and evolution of the Kenticha Rare-element
904 granite-pegmatite, Adola, Ethiopia. Journal of African Earth Sciences 162, 103691.
905 Blasband, B., White, S., Brooijmans, P., De Broorder, H., Visser, W., 2000. Late Proterozoic
906 extensional collapse in the Arabian-Nubian Shield. Journal of Geological Society of
907 London 157, 615-628.
908 Bonin, B., 2007. A-type granites and related rocks: Evolution of a concept, problems and prospects.
909 Lithos 97, 1-29.
910 Clarke, D.B., Rottura, A., 1994. Garnet-Forming and Garnet-Eliminating Reactions in a Quartz
911 Diorite Intrusion at Capo-Vaticano, Calabria, Southern Italy. Canadian Mineralogist 32,
912 623-635.
913 Clemens, J.D., Holloway, J.R., White, A.J.R., 1986. Origin of an A-type granite: experimental
914 constraints. American Mineralogist 71, 317-324.
915 Collins, W.J., Beams, S.D., White, A.J.R., Chappell, B.W., 1982. Nature and origin of A-type
916 granites with particular reference to southeastern Australia. Contributions to Mineralogy
917 and Petrology 80, 189-200.
918 Creaser, R.A., Price, R.C., Wormald, R.J., 1991. A-type granites revisited: assessment of a
919 residual-source model. Geology 19(2), 163–166.
920 Cuney, M., Marignac, C., Weisbrod, A., 1992. The Beauvoir topaz-lepidolite albite granite (Massif
921 Central France): the disseminated magmatic Sn–Li–Ta–Nb–Be mineralization. Economic
922 Geology 87, 1766–1794.
923 Dahlquist, J. A., Galindo, C., Pankhurst, R. J., Rapela, C. W., Alasino, P. H., Saavedra, J., Fanning,
924 C. M., 2007. Magmatic evolution of the Peñón Rosado granite: Petrogenesis of garnet-
925 bearing granitoids. Lithos 95, 177-207.

De la Roche, H., Leterrier, J., Grandclaude, P., Marchal, M., 1980. A classification of volcanic and plutonic rocks using R_1-R_2 diagrams and major-element analyses — its relationship with current nomenclature. Chemical Geology 29, 183-210.

Dorais, M.J., Tubrett, M., 2012. Detecting Peritectic Garnet in the Peraluminous Cardigan Pluton, New Hampshire. Journal of Petrology 53, 299-324.

Dostal, J., Chatterjee, A.K., 1995. Origin of topaz-bearing and related peraluminous granites of the late Devonian Davis Lake pluton, Nova Scotia, Canada: crystal versus fluid fractionation. Chemical Geology 123, 67–88.

du Bray, E.A., 1988. Garnet compositions and their use as indicators of peraluminous granitoid petrogenesis-southeastern Arabian Shield. Contributions to Mineralogy and Petrology 100, 205-212.

du Bray, E.A., 1994. Compositions of micas in peraluminous granitoids of the eastern Arabian Shield-implications for petrogenesis and tectonic setting of highly evolved, rare-metal enriched granites. Contributions to Mineralogy and Petrology 116, 381-397.

Eby, G.N., 1990. The A-type granitoids: A review of their occurrence and chemical characteristics and speculations on their petrogenesis. Lithos 26, 115-134.

Eby, G.N., 1992. Chemical subdivisions of the A-type granitoids: petrogenesis and tectonic implications. Geology 20, 641-644.

El-Galy, M.M., Khaleal, F.M., Bakhit, A.F., 2016. Comparative study on the geological and geochemical characteristics of some rare-metal granites, southeastern desert, Egypt. Nuclear Sciences Scientific Journal 5(1), 109-120.

El Hadek, H.H., Mohamed, M.A., El Habaak, G.H., Bishara, W.W., Ali, K.A., 2016. Geochemical Constraints on Petrogenesis of Homrit Waggat Rare Metal Granite, Egypt. International Journal of Geophysics and Geochemistry 3(4), 33-48.

Eliwa H. A., Ali K. G., Masoud S. M., Murata M., Abdel Gawad A. E. 2018, Geochemical features of granitoids at Nikeiba area, Eastern Desert, Egypt. XXIV All-Russian scientific conference “Ural Mineralogical School-2018”.

El-Tabal, H.K., 1979. Mineralogical studies on some rare metal apogranites from Nuweibi and Abu Dabbab areas, Eastern Desert, Egypt. MSc thesis, Al-Azhar University, Cairo, pp 112.

955 Emam, A., Zoheir, B., Radwan, A.M., Lehmann, B., Zhang, R., Fawzy, S., Nolte, N., 2018.
956 Petrogenesis and evolution of the Nuweibi rare-metal granite, Central Eastern Desert,
957 Egypt. Arabian Journal of Geosciences 11(23), 1-15.
958 Erdmann, S., Jamieson, R.A., MacDonald, M.A., 2009. Evaluating the Origin of Garnet,
959 Cordierite, and Biotite in Granitic Rocks: a Case Study from the South Mountain Batholith,
960 Nova Scotia. Journal of Petrology 50, 1477-1503.
961 Evensen, N.M., Hamilton, P.J., O'Nions, R.K., 1978. Rare earth abundances in chondritic
962 meteorites. Geochimica et Cosmochimica Acta 42(8), 1199-1212.
963 Farahat, E.S., Azer, M.K., 2011. Post-collisional magmatism in the northern Arabian-Nubian
964 Shield: the geotectonic evolution of the alkaline suite at Gebel Tarbush area, south Sinai,
965 Egypt. Chemie der Erde 71, 247-266.
966 Farahat, E.S., Mohamed, H.A., Ahmed, A.F., El Mahallawi, M.M., 2007. Origin of I- and A-type
967 granitoids from the Eastern Desert of Egypt: implications for crustal growth in the northern
968 Arabian-Nubian Shield. Journal of African Earth Science 49, 43-58.
969 Foord, E.E., Černý, P., Jackson, L.L., Sherman, D.M., Eby, R.K., 1995. Mineralogical and
970 geochemical evolution of micas from miarolitic pegmatites of the anorogenic Pikes Peak
971 Batholith, Colorado. Mineralogy and Petrology 55, 1-26.
972 Frost, B.R., Barnes, C.G., Collins, W.J., Arculus, R.J., Ellis, D.J., Frost, C.D., 2001. A geochemical
973 classification for granitic rocks. Journal of Petrology 42, 2033-2048.
974 Gahlan, H.A., Obeid, M.A., Azer, M.K., Asimow, P.D., 2018. An example of post-collisional
975 appinitic magmatism with an arc-like signature: the Wadi Nasb mafic intrusion, north
976 Arabian-Nubian Shield, south Sinai, Egypt. International Geology Review 60(7), 865–888.
977 Gaspar, M., Knaack, C., Meinert, L.D., Moretti, R., 2008. REE in skarn systems: A LA-ICP-MS
978 study of garnets from the Crown Jewel gold deposit. Geochimica et Cosmochimica Acta
979 72(1), 185-205.
980 Gualda, G.A.R., Ghiorso, M.S., 2014. Phase-equilibrium geobarometers for silicic rocks based on
981 rhyolite-MELTS. Part 1: Principles, procedures, and evaluation of the method.
982 Contributions to Mineralogy and Petrology 168(1), 1033.

983 Haapala, I., Frindt, S., Kandara, J., 2007. Cretaceous gross spitzkoppe and klein spitzkoppe stocks
984 in Namibia: topaz-bearing A-type granites related to continental rifting and mantle plume.
985 Lithos 97, 174-192.
986 Hackett, D., 1986. Mineralized aplite–pegmatite at Jabal Sa'id, Hijaz region, Kingdom of Saudi
987 Arabia. Journal of African Earth Sciences 4, 257–267.
988 Harangi, S., Downes, H., Kosa, L., Szabo, C., Thirlwall, M.F., Mason, P.R.D., Mattey, D., 2001.
989 Almandine garnet in calc-alkaline volcanic rocks of the northern Pannonian Basin (eastern-
990 central Europe): Geochemistry, petrogenesis and geodynamic implications. Journal of
991 Petrology 42, 1813-1843.
992 Hargrove, U.S., Stern, R.J., Kimura, J.-I., Manton, W.I., Johnson, P.R., 2006. How juvenile is the
993 Arabian-Nubian Shield? Evidence from Nd isotopes and pre-Neoproterozoic inherited
994 zircon in Bi'r Umk suture zone, Saudi Arabia. Earth Planetary Science Letters 252, 308-
995 326.
996 Harris, N.B., Pearce, J.A., Tindle, A.G., 1986. Geochemical characteristics of collision-zone
997 magmatism. In: Coward, M.P., Ries, A.C. (Eds.), Collision Tectonics. Journal of
998 Geological Society, London, Special Publication 19, pp. 67–81.
999 Hassanen, M.A. Harraz, H. Z., 1996. Geochemistry and Sr- and Nd-isotopic study on rare-metal-
1000 beating granitic rocks, central Eastern Desert, Egypt. Precambrian Research, 80, 1-22.
1001 Hassanen, M.A., Saad, N.A., Khalefa, O.M., 1995. Geochemical aspects and origin of Tin-bearing
1002 granites in the Eastern Desert, Egypt. Acta Mineralogica-Petrographica XXXVI, 55-72.
1003 Hawley, C.C., Wobus, R.A., 1977. General geology and petrology of the Precambrian crystalline
1004 rocks, Park and Jefferson Counties, Colorado. United States Geological Survey
1005 Professional Paper 608-B, 77 pp.
1006 Heikal, M.T.S., Khedr, M.Z., Abd El-Monsef, M., and Gomaa, S.R., 2019. Petrogenesis and
1007 geodynamic evolution of Neoproterozoic Abu Dabbab Albite Granite, Central Eastern
1008 Desert of Egypt: Petrological and geochemical constraints. Journal of African Earth
1009 Sciences 158, 103518.
1010 Helba, H., Trumbull, R.B., Morteani, G., Khalil, S.O., Arslan, A., 1997. Geochemical and
1011 petrographic studies of Ta mineralization in the Nuweibi albite granite complex, Eastern
1012 Desert, Egypt. Mineralium Deposita 32(2), 164–179.

1013 Higgins, N.C., Solomon, M., Varne, R., 1985. The genesis of the Blue Tier Batholith, northeastern
1014 Tasmania, Australia. Lithos 18, 129–149.
1015 Holtz, F., Behrens, H., Dingwell, D.B., and Taylor, R.P., 1992. Water solubility in aluminosilicate
1016 melts of haplogranite composition at 2 kbar. Chemical Geology, 96, 289–302.
1017 Irber, W., 1999. The lanthanide tetrad effect and its correlation with K/Rb, Eu/Eu*, Sr/Eu, Y/Ho,
1018 and Zr/Hf of evolving peraluminous granite suites. Geochimica et Cosmochimica Acta, 63:
1019 89–508.
1020 Jahn, B.-M., Wu, F.Y., Capdevila, R., Martineau, F., Zhao, Z., Wang, Y., 2001. Highly evolved
1021 juvenile granites with tetrad REE patterns: the Woduhe and Baerzhe granite from the Great
1022 Xing'an Mountains in NE China. Lithos 59, 171-198.
1023 Jahn, S., 1996. Geochemische und mineralogische Untersuchungen zur Metallogenese
1024 Seltenmetall-führen der Granitoide in der Central Eastern Desert, Ägypten. Unpubl. Ph.D
1025 thesis, Technische Universität Berlin, 271 pp.
1026 Johnson, P.R., 2003. Post-amalgamation basins of the NE Arabian shield and implications for
1027 Neoproterozoic III tectonism in the northern East African orogen. Precambrian Research
1028 123, 321-338.
1029 Johnson, P.R., Halverson, G.P., Kusky, T.M., Stern, R.J., Pease, V., 2013. Volcano-sedimentary
1030 Basins in the Arabian-Nubian Shield: Markers of Repeated Exhumation and Denudation in
1031 a Neoproterozoic Accretionary Orogen. Geosciences 3, 389-445.
1032 Kamel, O.A., El Tabbal, H.K., 1980. Petrology and mineralogy of Nuweibi and Abu Dabbab rare
1033 metal apogranites, Eastern Desert, Egypt. Proc. Geodynamic Evolution of the Afro-Arabic
1034 Rift System, Atti. Cony. Lincei. 47, 685-705, Roma.
1035 Khaleal, F., Rashed, M., & Saleh, W. (2007). Uranium potentiality Of Gabal Nikeiba Area, South
1036 Eastern Desert, Egypt. Fifth International Conference on the Geology of Africa 1, 41-45.
1037 Khalil, A.E.S., Obeid, M.A., Azer, M.K., 2015. Late Neoproterozoic post-collisional mafic
1038 magmatism in the Arabian–Nubian Shield: A case study from Wadi El-Mahash gabbroic
1039 intrusion in southeast Sinai, Egypt. Journal of African Earth Sciences 105, 29-46.
1040 Khalil, A.E.S., Obeid, M.A., Azer, M.K., Asimow, P.D., 2018. Geochemistry and petrogenesis of
1041 post-collisional alkaline and peralkaline granites of the Arabian-Nubian Shield: a case study

from the southern tip of Sinai Peninsula, Egypt. International Geology Review 60(8), 998-1018.

Kile, D.E., Foord, E.E., 1998. Micas from the Pikes Peak Batholith and its cogenetic granitic pegmatites, Colorado: Optical properties, composition, and correlation with pegmatite evolution. The Canadian Mineralogist 36, 463-482.

King, P.L., White, A.J.R., Chappell, B.W., Allen, C.M., 1997. Characterization and origin of aluminous A-type granites from the Lachlan Fold Belt, southeastern Australia. Journal of Petrology 38, 371-391.

Kontak, D.J., Corey, M., 1988. Metasomatic Origin of Spessartine-Rich Garnet in the South Mountain Batholith, Nova-Scotia. Canadian Mineralogist 26, 315-334.

Küster, D., 2009. Granitoid-hosted Ta mineralization in the Arabian–Nubian Shield: ore deposit types, tectono-metallogenetic setting, and petrogenetic framework. Ore Geology Reviews 35, 68–86.

Levillain, C., Maurel, P., Menil, F., 1981. Mössbauer studies of synthetic and natural micas on the polylithionite-siderophyllite join. Physics and Chemistry of Minerals 7 ,71-76.

Li, J., Huang, X.-L., Fu, Q., Li, W.-X., 2021. Tungsten mineralization during the evolution of a magmatic-hydrothermal system: Mineralogical evidence from the Xihuashan rare-metal granite in South China. American Mineralogist 106, 443-460.

Li, X.H., Li, Z.X., Li, W.X., Liu, Y., Yuan, C., Wei, G.J., Qi, C.S., 2007. U-Pb zircon, geochemical and Sr–Nd–Hf isotopic constraints on age and origin of Jurassic I and A-type granites from central Guangdong, SE China: a major igneous event in response to foundering of a subducted flat-slab? Lithos 96 (1–2), 186–204.

Liégeois, J.P., Black, R., 1987. Alkaline magmatism subsequent to collision in the Pan-African belt of the Adrar des Iforas. In: Fitton, J.G., Upton, B.G.J. (Eds.), Alkaline Igneous Rocks. Geological Society, Special Publication 30, 381-401.

Liégeois, J.P., Navez, J., Black, R., Hertogen, J., 1998. Contrasting origin of post-collision high-K calc-alkaline and shoshonitic versus alkaline and peralkaline granitoids. The use of sliding normalization. Lithos 45, 1-28.

1070 Liégeois, J.P., Stern, R.J., 2010. Sr–Nd isotopes and geochemistry of granite-gneiss complexes
1071 from the Meatiq and Hafafit domes, Eastern Desert, Egypt: no evidence for pre-
1072 Neoproterozoic crust. Journal of African Earth Sciences 57(1-2), 31–40.
1073 London, D., 2015. Reading pegmatites: Part 1—What beryl says. Rocks and Minerals 90(2), 138-
1074 153.
1075 Maniar, P.D., Piccoli, P.M., 1989. Tectonic discrimination of granitoids. Geological society of
1076 America Bulletin 101(5), 635-643.
1077 Manning, D.A.C., 1981. The effect of fluorine on liquidus phase relationships in the system Qz-
1078 Ab-Or with excess water at 1 kb. Contributions to Mineralogy and Petrology 76, 206-215.
1079 McCarthy, T.S., Fripp, R.E.P., 1980. The crystallization history of a granitic magma, as revealed
1080 by trace element abundances. Journal of Geology 88, 211 – 224.
1081 Meert, J.G., 2003. A synopsis of events related to the assembly of eastern Gondwana.
1082 Tectonophysics 362, 1-40.
1083 Miller, C.F., Stoddard, E.F., Bradfish, L.J., Dollase, W.A., 1981. Composition of plutonic
1084 muscovite: genetic implications. Canadian Mineralogist 19(1), 25-34.
1085 Moghazi, A.M., Harbi, H.M., Ali, K.A., 2011. Geochemistry of the Late Neoproterozoic Hadb adh
1086 Dayheen ring complex, Central Arabian Shield: Implications for the origin of rare-metal-
1087 bearing post-orogenic A-type granites. Journal of Asian Earth Sciences 42(6), 1324-1340.
1088 Moghazi, A.K.M., Iaccheri, L.M., Bakhsh, R.A., Kotov, A.B., Ali, K.A., 2015. Sources of rare-
1089 metal-bearing A-type granites from Jabel Sayed complex, Northern Arabian Shield, Saudi
1090 Arabia. J. Asian Earth Sci. 107, 244–258.
1091 Mohamed, M.A., El-Habaak, G.H., Bishara, W.W., El-Hadek, H.H., 2009. Geochemistry and
1092 microthermometry of Homr Akarem and Homret Mikipid rare-metal granites, south Eastern
1093 Desert, Egypt. The Sixth International Conference on the Geology of Africa, 61-87.
1094 Mohamed, M.A., El-Habaak, G.H., Bishara, W.W., El-Hadek, H.H., 2009b.Geochemical and fluid
1095 inclusions studies on fluorite mineralization at Homr Akarem and Homret Mikpid granites,
1096 south Eastern Desert, Egypt. Mansoura journal of Biology 36 (2), 227-241.
1097 Monier, G., Robert, J.-L., 2018. Evolution of the miscibility gap between muscovite and biotite
1098 solid solutions with increasing lithium content: An experimental study in the system K_2O-

1099 Li_2O-MgO-FeO-Al_2O_3-SiO_2-H_2O-HF at 600°C, 2 kbar P_{H_2O}: Comparison with natural
1100 lithium micas. Mineralogical Magazine 50(358). 641-651.
1101 Montel, J.M., Vielzeuf, D., 1997. Partial melting of metagreywackes, Part II. Compositions of
1102 minerals and melts. Contribution to Mineralogy and Petrology 128, 176-196.
1103 Morsy M.A., Mohamed, F.H., 1992. Geochemical characteristics and petrogenetic aspects of
1104 Mueilha tin-specialized granite, Eastern Desert, Egypt. Bulletin of Faculty of Science,
1105 Alexandria University, Egypt 32(A), 502–515.
1106 Moufti, A.M., Ali, K.A., Whitehouse, M.J., 2013. Geochemistry and petrogenesis of the Ediacaran
1107 post-collisional Jabal Al-Hassir ring complex, Southern Arabian Shield, Saudi Arabia.
1108 Geochemistry 73(4), 451-67.
1109 Munoz, J. L., & Ludington, S. (1977). Fluorine-hydroxyl exchange in synthetic muscovite and its
1110 application to muscovite-biotite assemblages. American Mineralogist, 62(3-4), 304-308.
1111 Nachit, H., Ibhi, A., Ohoud, M.B., 2005. Discrimination between primary magmatic biotites,
1112 reequilibrated biotites and neoformed biotites. Comptes Rendus Geoscience, 337 (16),
1113 1415-1420.
1114 Nurmi, P.A., Haapala, I., 1986. The Proterozoic granitoids of Finland: granite types, metallogeny
1115 and relation to crustal evolution. Bulletin of the Geological Society of Finland 58, 203-233.
1116 Obeid, M.A., Azer, M.K., 2015. Pan-African adakitic rocks of the north Arabian-Nubian Shield:
1117 petrological and geochemical constrains on the evolution of the Dokhan volcanics in the
1118 north Eastern Desert of Egypt. International Journal of Earth Sciences 104, 541-563.
1119 Patiño Douce, A.E., 1997. Generation of metaluminous A-type granites by low pressure melting
1120 of calc-alkaline granitoids. Geology 25(8), 743–746.
1121 Patiño Douce, A.E., 1999. What do experiments tell us about the relative contributions of crust and
1122 mantle to the origin of granitic magmas? In: Castro, A., Fernandez, C., Vigneresse, J. (eds)
1123 Understanding Granites: Integrating New and Classical Techniques. Geological Society,
1124 London, Special Publications 168, 55-75.
1125 Pearce, J.A., Harris, N.B.W., Tindle, A.G., 1984. Trace element discrimination diagrams for the
1126 tectonic interpretation of granitic rocks. Journal of Petrology 25, 956-983.
1127 René, M., Stelling, J., 2007. Garnet-bearing granite from the Třebíč pluton, Bohemian Massif
1128 (Czech Republic). Mineralogy and Petrology 91, 55-69.

Renno, A., 1997. Zur Petrogenese der Albitgranite von Abu Dabbab und Nuweibi, Central Eastern Desert, Ägypten. Unpubl PhD thesis, Technische Universität Berlin, 216 pp.

Riad, A.M., 1979. Geology and petrology on some apogranite occurrence, Nuweibi area, Eastern Desert, Egypt. M Sc Thesis, Al-Azhar University, Cairo, Egypt.

Rino, S., Kon, Y., Sato, W., Maruyama, S., Santosh, M. and Zhao, D., 2008. The Grenvillian and Pan-African orogens: world's largest orogenies through geologic time, and their implications on the origin of super plume. Gondwana Research 14(1-2), 51-72.

Sabet, A.H., Tsogoev, V.B., Babourin, L.M., Riad, A.M., Zakhari, A., Armanius, L.K., 1976. Geologic structure and laws of localization of tantalum mineralization at the Nuweibi deposit. Annals of Geological Survey of Egypt 6, 119-156.

Sami, M., Ntaflos, T., Mohamed, H.A., Farahat, E S, Hauzenberger, C., Mahdy, N.M., Abdelfadil, K.M., Fathy, D., 2020. Origin and petrogenetic implications of spessartine garnet in highly fractionated granite from the central Eastern Desert of Egypt. Acta Geologica Sinica-English Edition 94(3), 763-776.

Schmitz, C., Burt, D.M., 1990. The Black Pearl mine, Arizona: Wolframite veins and stockscheider pegmatite related to an albitic stock. Special Paper - Geological Society of America 246, 221–232.

Seddik, A.M., Darwish, M.H., Azer, M.K., Asimow, P.D., 2020. Assessment of magmatic versus post-magmatic processes in the Mueilha rare-metal granite, Eastern Desert of Egypt, Arabian-Nubian Shield. Lithos, 105542.

Skjerlie, K.P., Johnston, A.D., 1993. Fluid-absent melting behavior of an F-rich tonalitic gneiss at mid-crustal pressures: implications for the generation of anorogenic granites. Journal of petrology 34(4), 785–815.

Smirnov, V.I., Ginzburg, A.I., Grigoriev, V.M. and Yakovlev, G.F. (1983) Studies of Mineral Deposits. Mir Pub., Moscow.

Stern, R.J., 1994. Arc assembly and continental collision in the Neoproterozoic East African Orogen: implications for the consolidation of Gondwanaland. Annual Reviews of Earth and Planetary Science 22, 319-351.

Stern, R.J., Hedge, C.E., 1985. Geochronologic constraints on late Precambrian crustal evolution in the Eastern Desert of Egypt. American Journal of Science 285, 97-127.

1159 Stoeser, D.B., Frost, C.D., 2006. Nd, Pb, Sr, and O isotopic characterization of Saudi Arabian
1160 Shield terranes. Chemical Geology 226, 163-188.
1161 Sun, S., McDonough, W.F., 1989. Chemical and isotopic systematic of oceanic basalts:
1162 implications for mantle compositions and processes. Magmatism in the Ocean Basins: In:
1163 Saunders AD, Norry MJ (eds.), Geological Society of London, Special Publications 42,
1164 313-345.
1165 Sylvester, P.J., 1989. Post-collisional alkaline granites. Journal of Geology 97(3), 261-280.
1166 Taylor, J., Stevens, G., 2010. Selective entrainment of peritectic garnet into S-type granitic
1167 magmas: evidence from Archaean mid-crustal anatectites. Lithos 120(3-4), 277-292.
1168 Villaros, A., Stevens, G., Buick, I.S., 2009. Tracking S-type granite from source to emplacement:
1169 clues from garnet in the Cape granite suite. Lithos 112, 217–235.
1170 Wang, R.C., Wu, F.Y., Xie, L., Liu, X.C., Wang, J.M., Yang, L., Lai, W., Liu, C., 2017. A
1171 preliminary study of rare-metal mineralization in the Himalayan leucogranite belts, South
1172 Tibet. Science China Earth Sciences 60, 1655–1663.
1173 Whalen, J.B., Currie, K.L., Chappell, B.W., 1987. A-type granites: geochemical characteristics,
1174 discrimination and petrogenesis. Contributions to Mineralogy and Petrology 95(4), 407-
1175 419.
1176 Whitworth, M.P., 1992. Petrogenetic implications of garnets associated with lithium pegmatites
1177 from SE Ireland. Mineralogical Magazine 56, 75–85.
1178 Winkler, H.G.F., Boese, M., and Marcopoulos, T., 1975. Low temperature granite melts. Neues
1179 Jahrbuch für Mineralogie. Monatshefte, 6, 245–268.
1180 Wu, F.Y., Liu, X.C., Liu, Z.C., Wang, R.C., Xie, L., Wang, J.M., Ji, W.Q., Yang, L., Liu, C.,
1181 Khanal, G.P., He, S.X., 2020. Highly fractionated Himalayan leucogranites and associated
1182 rare-metal mineralization. Lithos 352-353, 105319.
1183 Wu, F.-Y., Sun, D.-y., Li, H., Jahn, B.-M., Wilde, S., 2002. A-type granites in northeastern China:
1184 age and geochemical constraints on their petrogenesis. Chemical Geology 187, 143–173.
1185 Yang, J.H., Peng, J.T., Hu, R.Z., Bi, X.W., Zhao, J.H., Fu, Y.Z., Shen, N.P., 2013. Garnet
1186 geochemistry of tungsten-mineralized Xihuashan granites in South China. Lithos 177, 79-
1187 90.

Yang, J.H., Wu, F.Y., Chung, S.L., Wilde, S.A., Chu, M.F., 2006. A hybrid origin for the Qianshan A-type granite, northeast China: geochemical and Sr–Nd–Hf isotopic evidence. Lithos 89(1–2), 89–106.

Zhang, J., Ma, C., She, Z., 2012. An Early Cretaceous garnet-bearing metaluminous A-type granite intrusion in the East Qinling Orogen, central China: petrological, mineralogical and geochemical constraints. Geoscience Frontiers 3, 636–646.

Zoheir, B., Lehmann, B., Emam, A., Radwan, A., Zhang, R., Bain, W.M., Steele-MacInnis, M., Nolte, N., 2020. Extreme fractionation and magmatic–hydrothermal transition in the formation of the Abu Dabbab rare-metal granite, Eastern Desert, Egypt. Lithos 352, 105329.

Figure captions

Figure 1. (a) General geologic map of the central and southern sectors (dividing line after Stern and Hedge, 1985) of the Eastern Desert of Egypt showing the locations of the most important rare-metal bearing granite intrusions: (1) Umm Naggat, (2) Umm Samra, (3) Abu Dabbab, (4) Nuweibi, (5) Ineiga, (6) Homrit Waggat, (7) Igla, (8) Zabara, (9) Mueilha, (10) Nugrus, (11) El-Gharabiya, (12) Nikeiba, (13) Homrit Akarem (the study area is marked by a blue box), and (14) Um Ara. (b) Aerial photo of the Homrit Akarem area showing the topographic expression of the Homrit Akarem intrusion into darker metasedimentary rocks; note the image has not been orthorectified and there is some geometric distortion especially towards the northern edge. (c) Geologic map of the Homrit Akarem area (after Hassanen and Harraz, 1996); the petrological sub-types of the Homrit Akarem Granitic Intrusion are not divided on this map. Precise sample locations for this study are indicated and GPS coordinates are given in Table 2. (d) Schematic cross-section (2x vertical exaggeration) showing the field relationships between the different rock types of the Homrit Akarem intrusion and their country rocks. Note line of section marked on Fig. 1c.

Figure 2. Field photographs: (a) metasedimentary xenolith in granodiorite, (b) Homrit Akarem granite intruded into metasedimentary country rock with a narrow hornfels contact aureole, (c) granodiorite xenolith within muscovite granite, (d) albite granite above the muscovite

granite, forming the apical portion of the Homrit Akarem pluton, and (f) highly tectonized granite with development of many fractures.

Figure 3. Petrographic features (a, e, and g in cross-polarized transmitted light; f and j in plane-polarized transmitted light; b, c, d, h and i are backscattered electron images): (a) zircon inclusion in quartz, (b) columbite inclusion in albite, (c) columbite inclusion in biotite (note tiny spot of brighter Ta-rich columbite at rim), (d) disseminated columbite crystal among other minerals, (e) coarse muscovite crystal altered on its boundaries to secondary muscovite, (f) subhedral garnet with crackly appearance and quartz inclusions, (g) topaz crystals with perfect cleavage corroded by microcline with small muscovite flake, (h) columbite associated with biotite and altered along margins into fluorcalciomicrolite and rhodochrosite, (i) columbite interstitial to feldspars broken and altered along margins into fluorcalciomicrolite and rhodochrosite, and (j) oscillatory color-banding in cassiterite with muscovite flakes and fluorite in greisen. The mineral abbreviations are: Qz = quartz, Zr = zircon, Mu = muscovite, Grt = garnet, Mc = microcline, To = topaz, Cs = cassiterite, Fl = fluorite, and Pl = plagioclase, Col= columbite, Fcm = fluorcalciomicrolite, Rc = rhodochrosite.

Figure 4. Mineral chemistry of HAGI samples. (a) TiO_2-($FeO_{(t)}$+MnO)-MgO ternary diagram for classification of biotite (after Nachit et al. 2005). (b) $FeO_{(t)}$ vs. Al_2O_3 discrimination diagram for biotite (Abdel-Rahman, 1994). (c) Mössbauer spectrum and peak-fitting for zinnwaldite from pink granite sample HAK9. The data are fitted with two doublets, assigned respectively to single Fe^{2+} and Fe^{3+} sites (Table 1). There is no evidence of ferromagnetic contamination. (d) "Foster diagram" for zinnwaldite after Foord et al. (1995). The vertices represent fractions of the octahedral site occupancy by Li, by trivalent cations and Ti (R^{3+} = Al+Ti+Fe^{3+}), and by divalent cations (R^{3+} = Fe^{2+}Mn+Mg+Zn). Data shown in black symbols are from the Pikes Peak Batholith, Colorado USA (Foord et al., 1995 unless otherwise indicated): filled triangles – annite from Barker et al. (1975), plus signs – annite from Hawley and Wobus (1977), open square – phlogopite, open triangles – lithian biotite, filled circles – zinnwaldite (solid arrows represent core-rim zoning), hexagon –

ferroan lepidolite. HAGI data in blue circles. The curved dashed arrow is the evolution trend line of progressive fractionation for the Pikes Peak pegmatites proposed by Foord et al. (1995). Mineral species abbreviations: SID = siderophyllite $KFe^{2+}{}_2Al(Al_2Si_2)O_{10}(F,OH)_2$, PL = polylithionite $KLi_2Al(Si_4)O_{10}(F,OH)_2$, TL = trilithionite $KLi_{1.5}Al_{1.5}(AlSi_3)O_{10}(F,OH)_2$. (e) Mg-Ti-Na ternary diagram for the compositional fields of muscovite after (Miller et al., 1981). (f) Chemical composition and nomenclature of the columbite-tantalite group minerals based on Ta/(Ta+Nb) vs. Mn/(Mn+Fe) ratios.

Figure 5. Nomenclature of the plutonic rocks using the R_1-R_2 diagram (De la Roche et al., 1980).

Figure 6. Variation diagrams of some major oxides against SiO_2. Symbols as shown in the legend of Fig. 5. On each panel, the r^2 and p statistics of a linear regression through the data are given. Values of $p < 0.01$ are considered statistically significant and are colored green. Cases where $0.01 \leq p < 0.02$ are marginally significant and are colored orange. Values of $p > 0.02$ indicate insignificant correlations and are colored red.

Figure 7. Variation diagrams of some trace elements against SiO_2. Symbols as shown in the legend of Fig. 5. Statistics of the regressions are shown as in Figure 6.

Figure 8. Normalized multi-trace element diagrams for whole-rock chemistry. (a) Primitive mantle normalized extended trace element diagram; normalization values from Sun and McDonough (1989). (b) Chondrite-normalized REE patterns; chondrite values from Evensen et al. (1978). Symbols as shown in the legend of Fig. 5.

Figure 9. Discrimination diagrams for magma type based on whole-rock chemistry. (a) $100*(MgO+FeO_{(t)}+TiO_2)/SiO_2$ vs. $(Al_2O_3+CaO)/(FeO_{(t)}+Na_2O+K_2O)$ for distinguishing between calc-alkaline, highly fractionated calc-alkaline, and alkaline granites (Sylvester, 1989). (b) Ga/Al vs. $FeO_{(t)}/MgO$ for distinguishing between I-, S-, or M-type and A-type granites (Whalen et al., 1987). (c) Ga/Al vs. Nb for distinguishing between I, S, M and A-

type granites (Whalen et al., 1987). (d) SiO_2 vs. Na_2O+K_2O-CaO (Frost et al., 2001). (e) Rb/Nb versus Y/Nb (Eby, 1992) with fields of A_1 and A_2 granitoids; A_1 are anorogenic A-type granites with mantle signatures whereas A_2 are post-collisional A-type granites with crustal sources. Symbols as shown in the legend of Fig. 5.

Figure 10. Tectonic discrimination diagrams based on whole-rock chemistry. (a) SiO_2 vs. Al_2O_3 after Maniar and Piccoli (1989). (b) Y+Nb vs. Rb (Pearce et al., 1984); note that the dashed line marks the extreme upper limit of "anomalous" ocean ridge granites, which is not relevant in the current case. (c) R_1-R_2 multicationic diagram (Batchelor and Bowden,1985). (d) Hf-Rb/30-3*Ta ternary diagram (after Harris et al., 1986). Abbreviations: R_1=4Si-11(Na+K)-2(Fe+Ti); R_2=6Ca+2Mg+Al; VAG: volcanic-arc granites; syn-COLG: syn-collisional granites; WPG: within-pate granites; ORG: ocean-ridge granites. Symbols as shown in the legend of Fig. 5.

Figure 11. (a) Rb/Sr vs. Sr. (b) Rb/Ba vs. Rb/Sr. (c) Rb vs. K/Rb. (d) Nb vs. Ta.

Figure 12. Normative composition of the HAGI samples plotted in Qz-Ab-Or projection. Dashed lines show the quartz-alkali feldspar cotectics and the trace of the water-saturated minimum melt compositions in the haplogranite system at total pressure ranging from 0.5 to 10 kbar (Holtz et al., 1992; Winkler et al., 1975). Solid cyan line shows the trace of the minimum melt composition at 1 kbar with excess H_2O and increasing fluorine (F) content up to 4 wt% F (Manning, 1981). The low normative quartz of the HAGI and other anorogenic granites is presumably a robust feature, whereas Ab/Or ratios are readily modified by hydrothermal activity. Independent measurement of the activity of F is necessary to distinguish the effects of pressure and F on controlling the major element chemistry of the magma.

Figure 13. Simplified model for the geodynamic evolution of the post-collisional HAGI (modified after Seddik et al., 2020): Lithospheric delamination triggers upwelling of asthenospheric mantle, generation of underplated basic magma, doming upwards and erosional unroofing of crust, partial melting of lower and middle crust, generation of A-type granitic magma,

ascent and emplacement of highly-fractionated magma extending to subvolcanic levels, and finally erosional removal of cover to expose the top of the pluton.

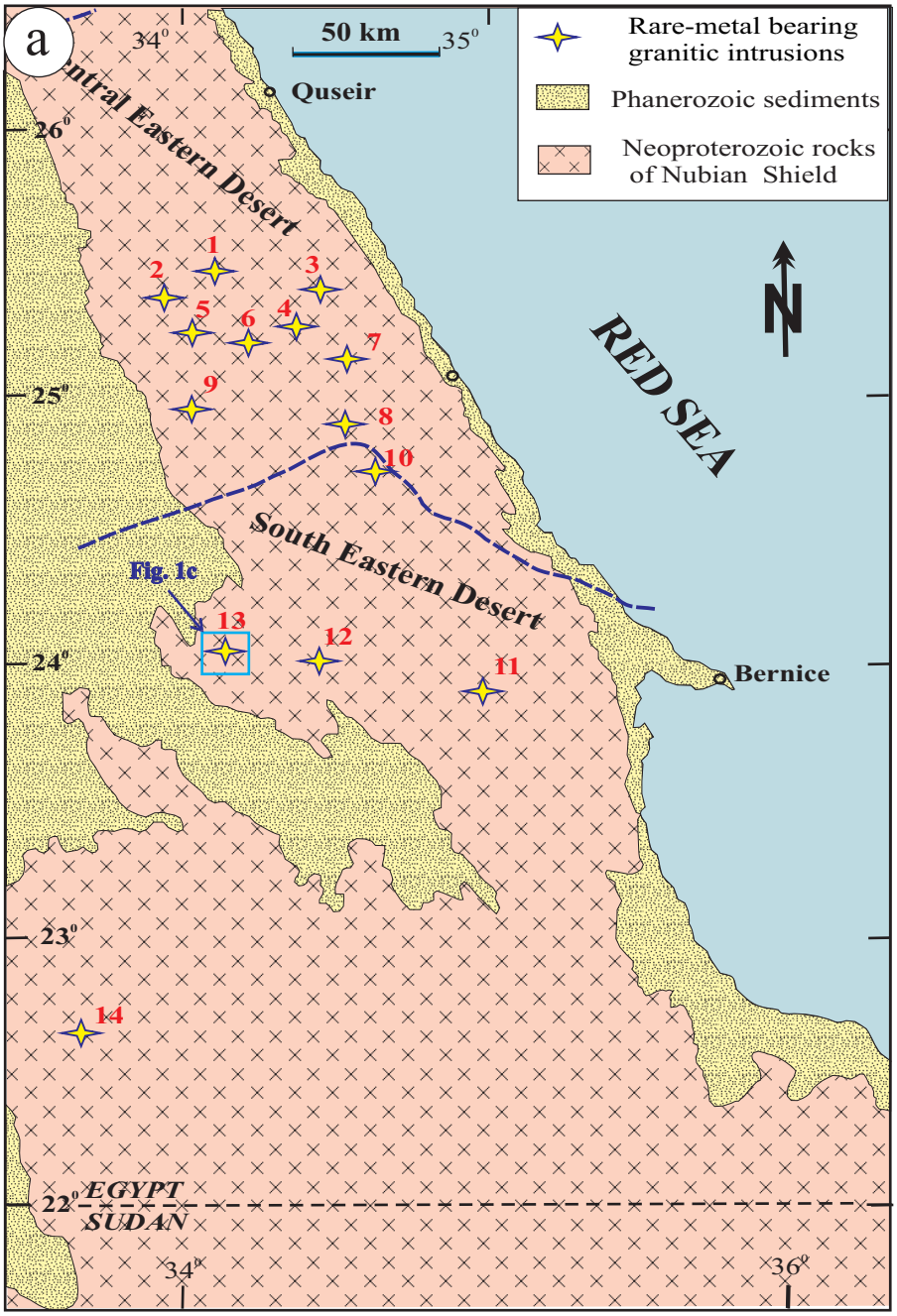
a
34°
35°
50 km
Quseir
Rare-metal bearing granitic intrusions
Phanerozoic sediments
Neoproterozoic rocks of Nubian Shield
N
RED SEA
Central Eastern Desert
South Eastern Desert
Fig. 1c
Bernice
26°
25°
24°
23°
22°
EGYPT
SUDAN
34°
36°
1
2
3
4
5
6
7
8
9
10
11
12
13
14

Figure 1a

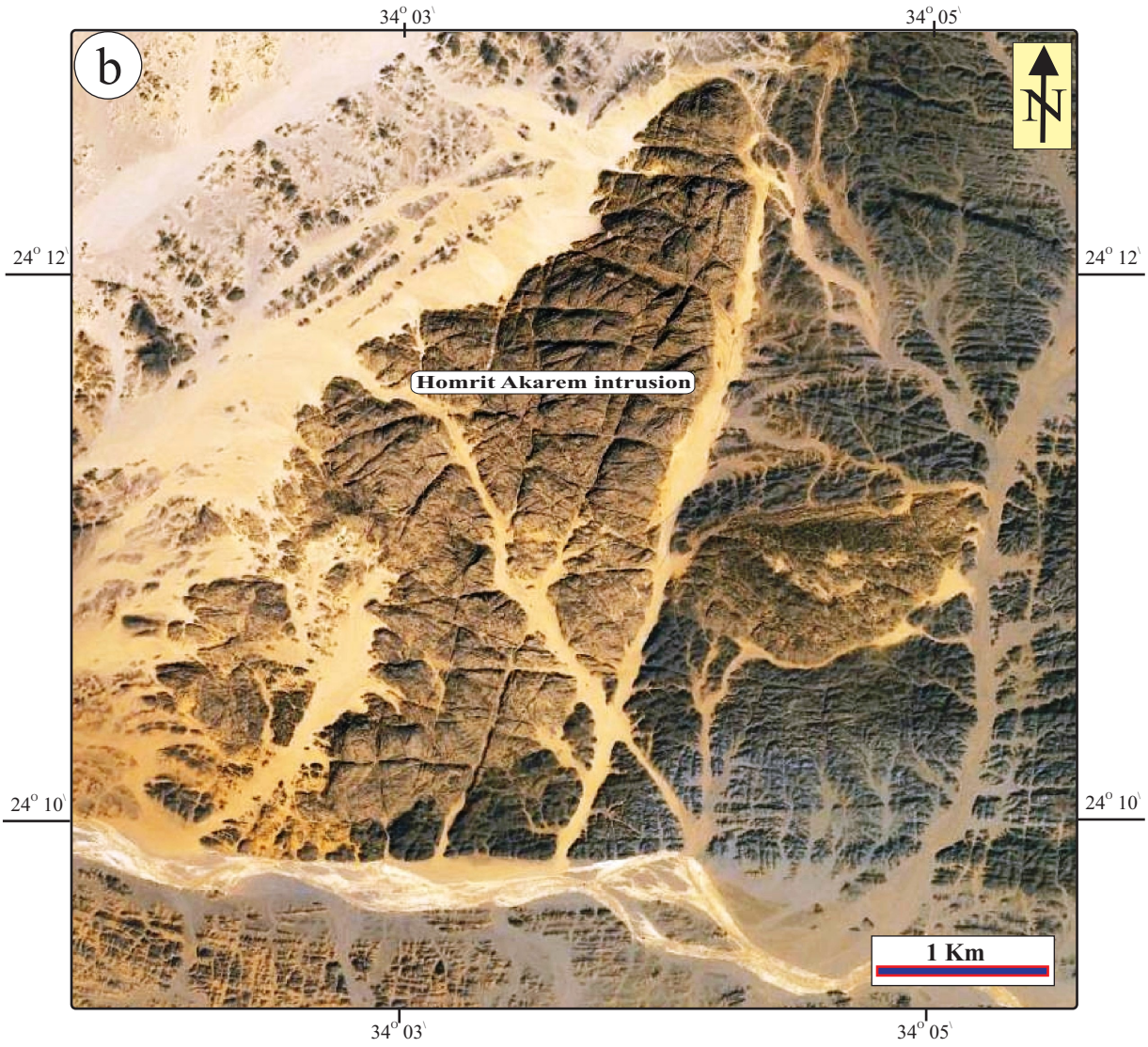

Figure 1b

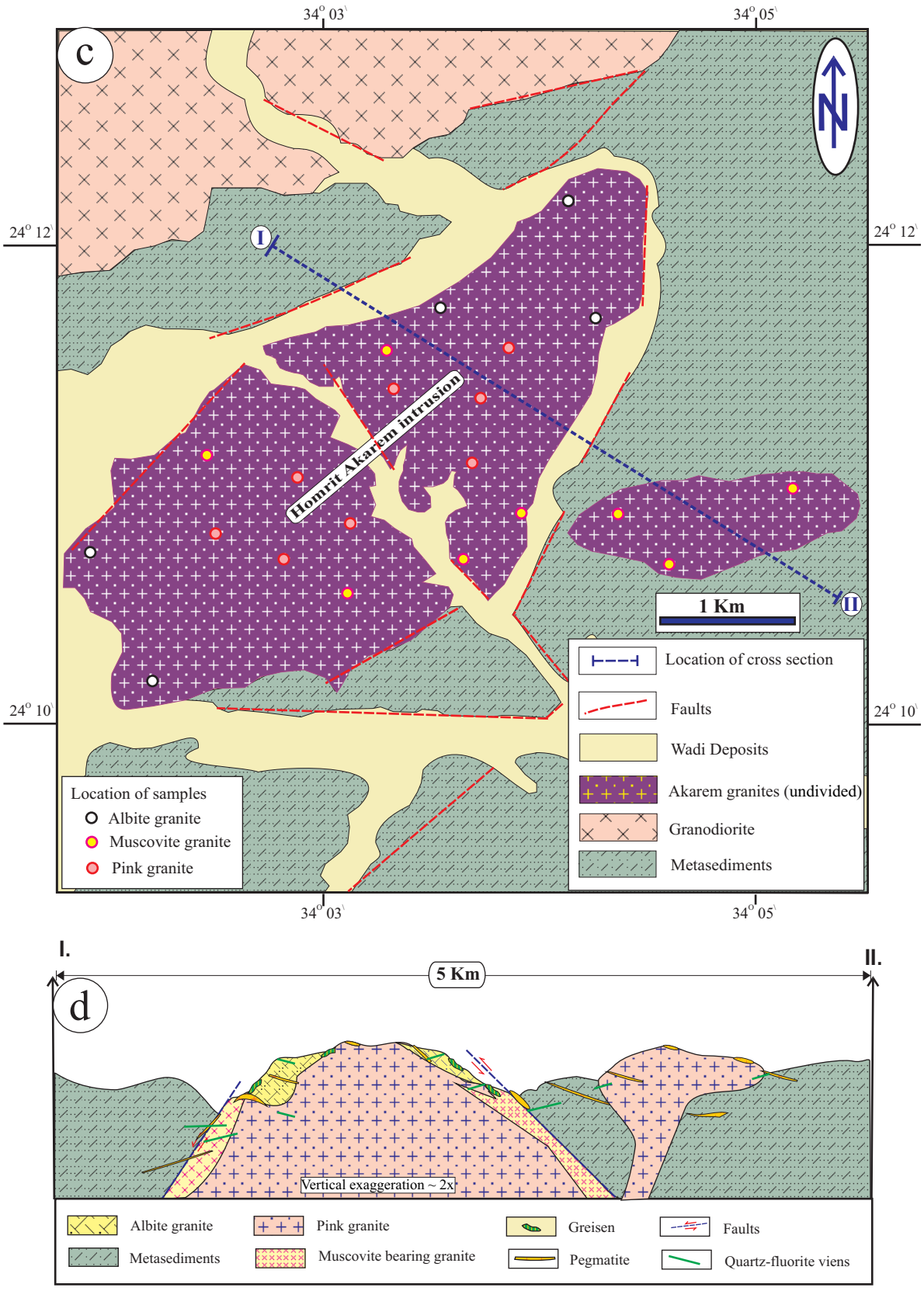
c
34° 03`
34° 05`
24° 12`
24° 10`
I
II
Homrit Akarem intrusion
1 Km
Location of cross section
Faults
Wadi Deposits
Akarem granites (undivided)
Granodiorite
Metasediments
Location of samples
Albite granite
Muscovite granite
Pink granite
I.
II.
5 Km
d
Vertical exaggeration ~ 2x
Albite granite
Pink granite
Greisen
Faults
Metasediments
Muscovite bearing granite
Pegmatite
Quartz-fluorite viens

Figure 1c, d

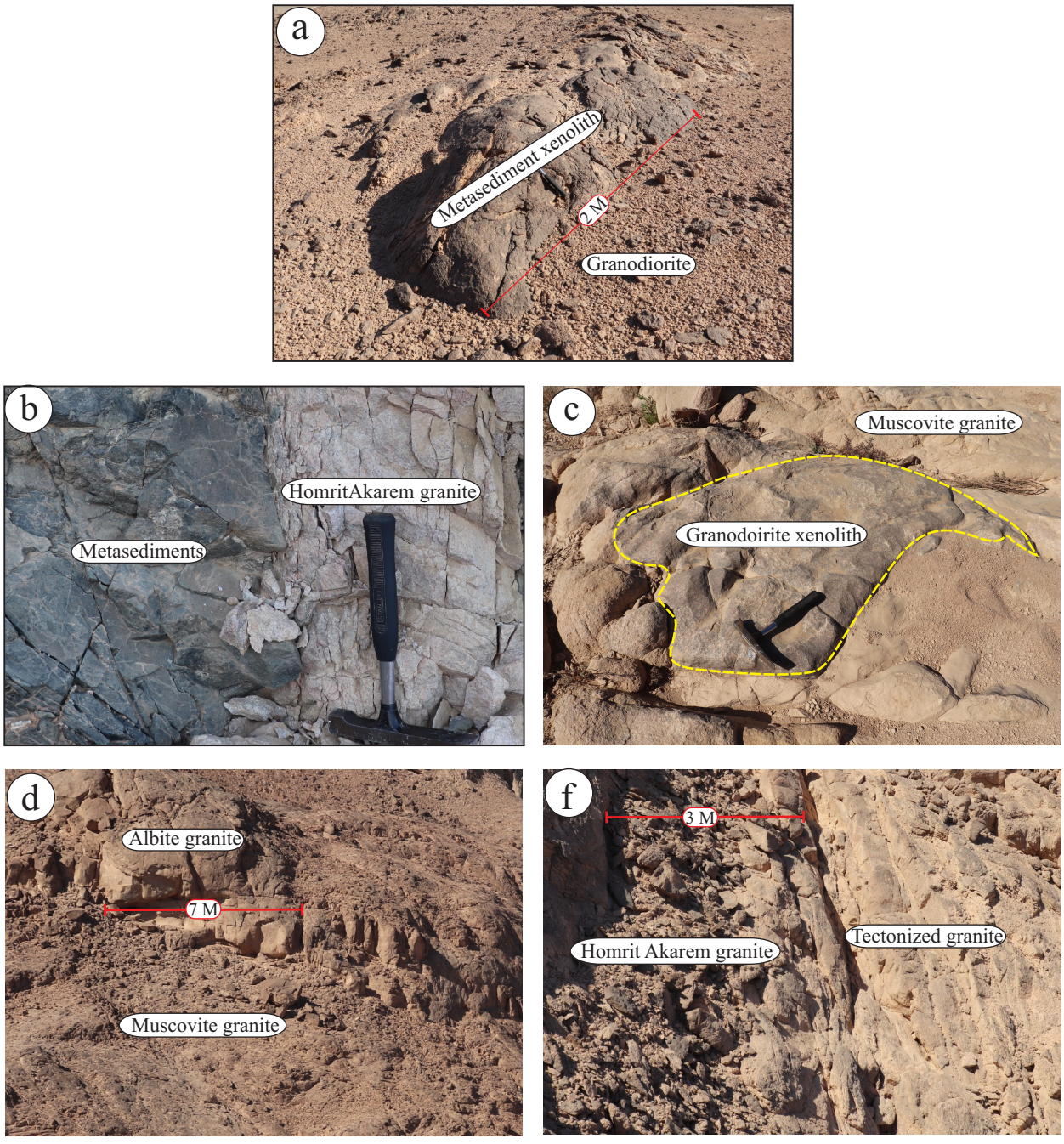
a
Metasediment xenolith
2 M
Granodiorite
b
HomritAkarem granite
Metasediments
c
Muscovite granite
Granodoirite xenolith
d
Albite granite
7 M
Muscovite granite
f
3 M
Homrit Akarem granite
Tectonized granite

Figure 2

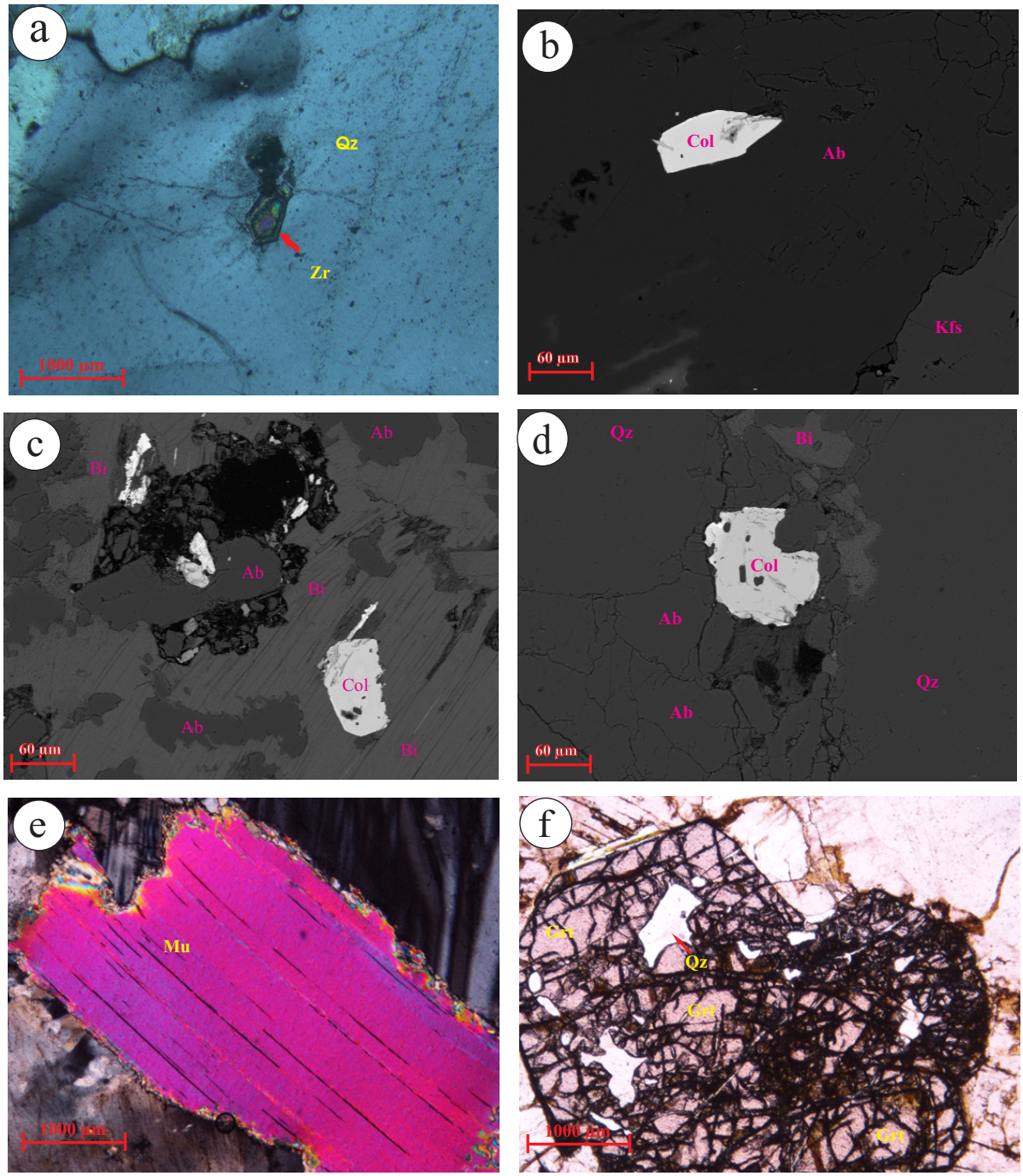
a
Qz
Zr
1000 µm
b
Col
Ab
Kfs
60 µm
c
Ab
Bi
Ab
Bi
Col
Ab
Bi
60 µm
d
Qz
Bi
Col
Ab
Qz
Ab
60 µm
e
Mu
1000 µm
f
Grt
Qz
Grt
1000 µm
Grt

Figure 3

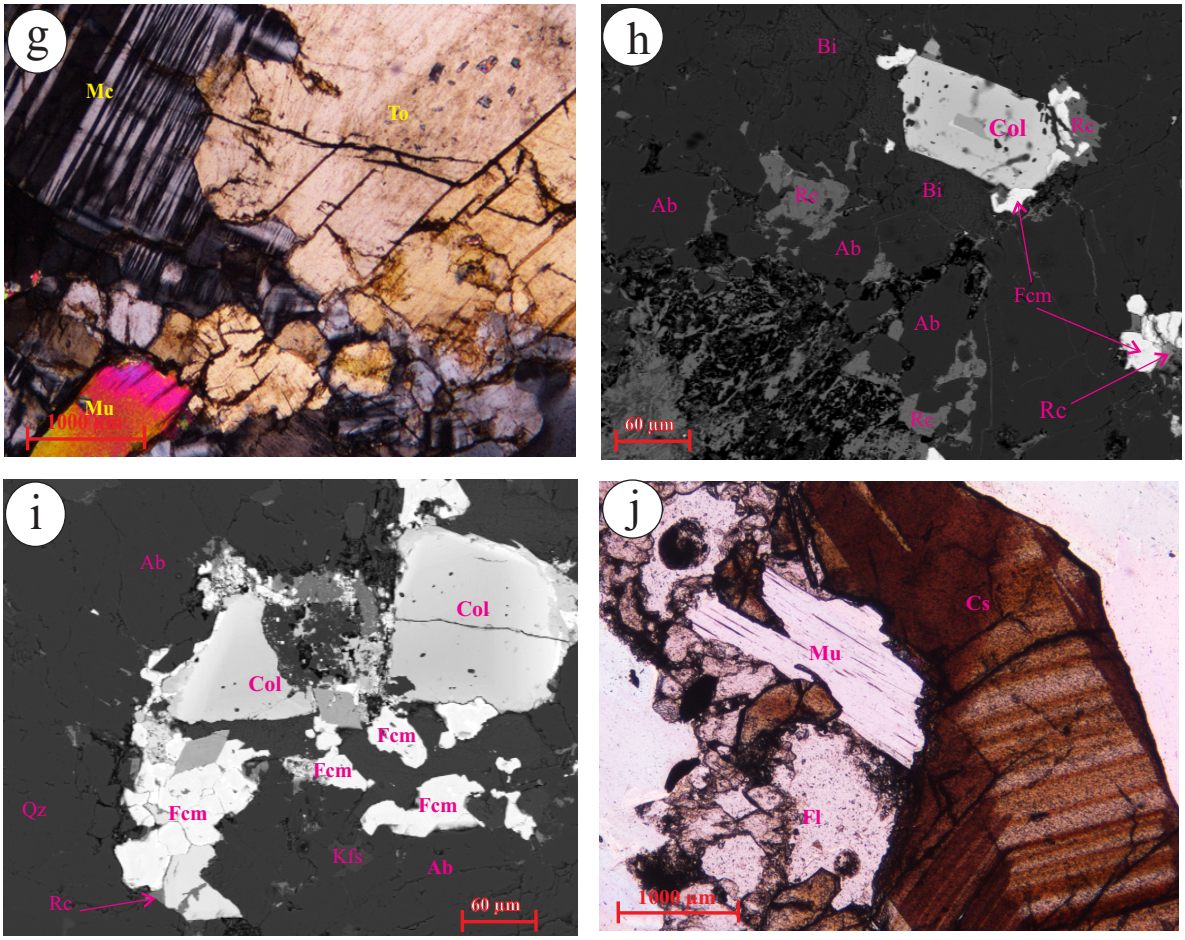

Figure 3 Cont.

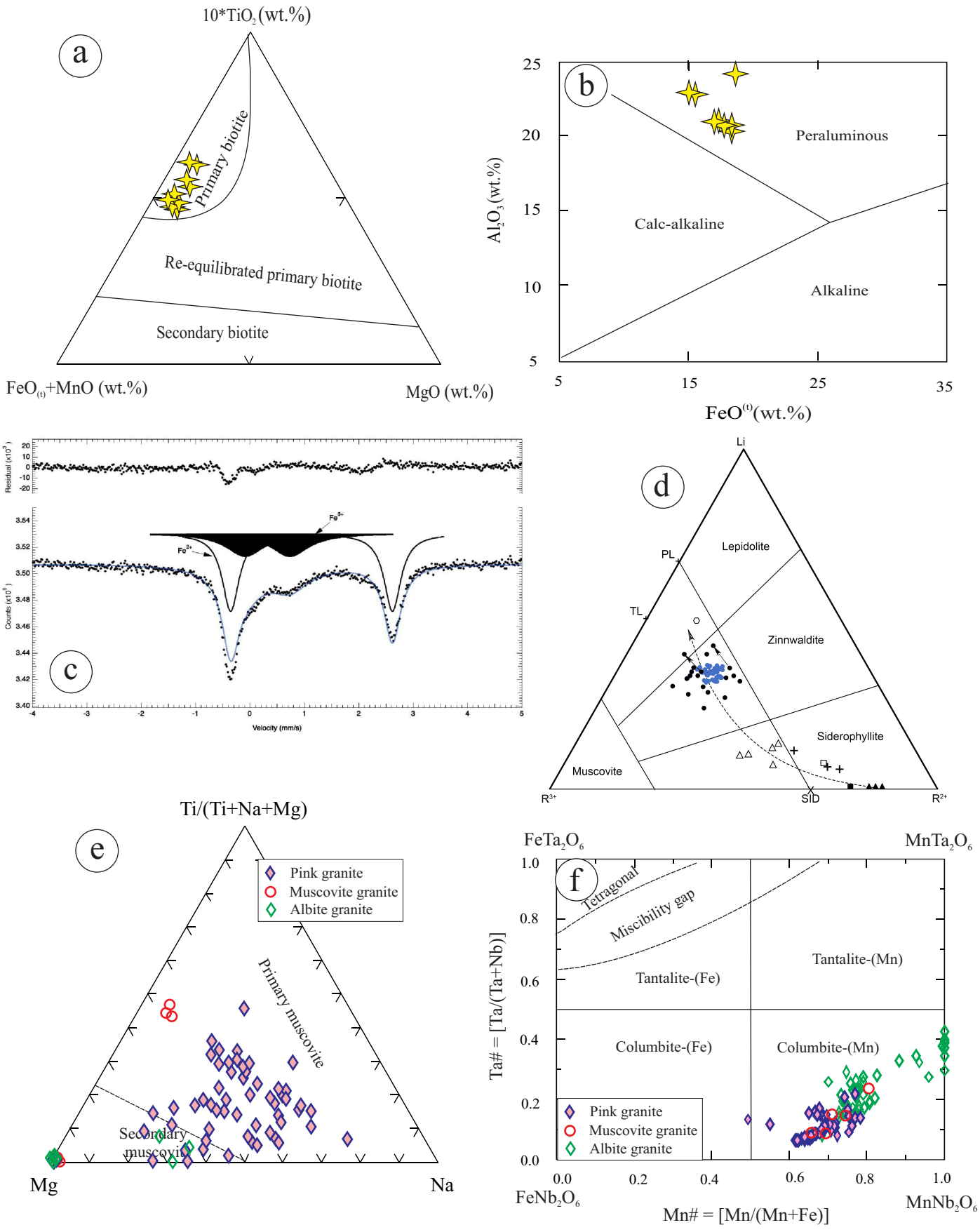
a
10*TiO2 (wt.%)
Primary biotite
Re-equilibrated primary biotite
Secondary biotite
FeO(t)+MnO (wt.%)
MgO (wt.%)
b
Peraluminous
Calc-alkaline
Alkaline
Al2O3 (wt.%)
FeO(t) (wt.%)
c
Residual (x10^3)
Fe3+
Fe2+
Counts (x10^6)
Velocity (mm/s)
d
Li
Lepidolite
PL
TL
Zinnwaldite
Siderophyllite
Muscovite
R3+
SID
R2+
e
Ti/(Ti+Na+Mg)
Pink granite
Muscovite granite
Albite granite
Primary muscovite
Secondary muscovite
Mg
Na
f
FeTa2O6
MnTa2O6
Tetragonal
Miscibility gap
Tantalite-(Mn)
Tantalite-(Fe)
Columbite-(Fe)
Columbite-(Mn)
Ta# = [Ta/(Ta+Nb)]
FeNb2O6
MnNb2O6
Mn# = [Mn/(Mn+Fe)]

Figure 4

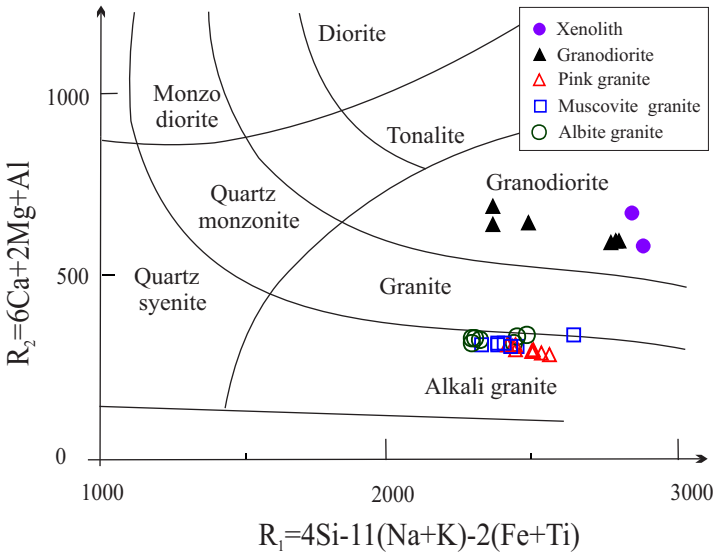
Xenolith
Granodiorite
Pink granite
Muscovite granite
Albite granite
Diorite
Monzo diorite
Tonalite
Granodiorite
Quartz monzonite
Quartz syenite
Granite
Alkali granite
1000
500
0
1000
2000
3000
R2=6Ca+2Mg+Al
R1=4Si-11(Na+K)-2(Fe+Ti)

Figure 5

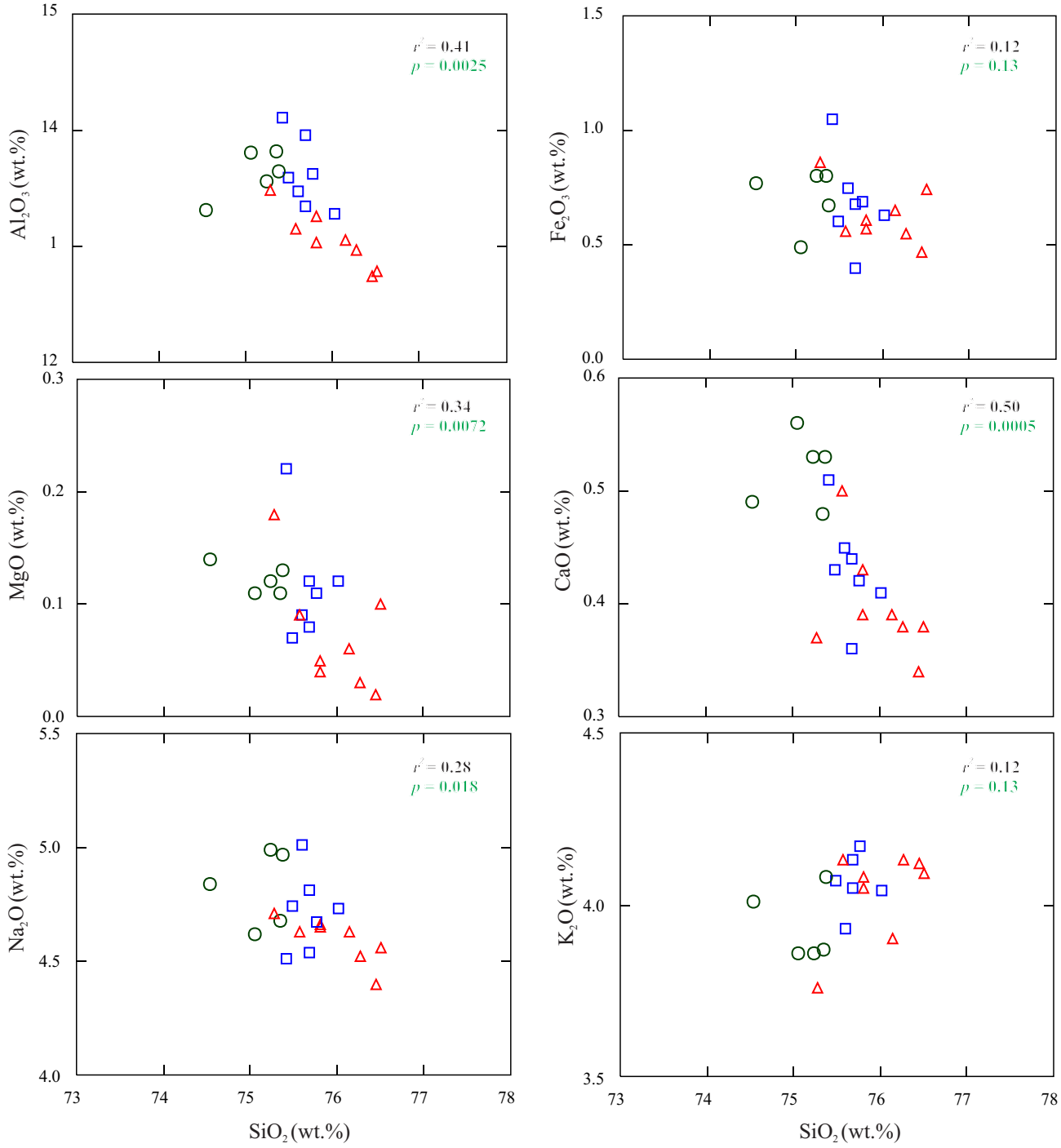
r^2 = 0.41
p = 0.0025
Al_2O_3 (wt.%)
r^2 = 0.12
p = 0.13
Fe_2O_3 (wt.%)
r^2 = 0.34
p = 0.0072
MgO (wt.%)
r^2 = 0.50
p = 0.0005
CaO (wt.%)
r^2 = 0.28
p = 0.018
Na_2O (wt.%)
r^2 = 0.12
p = 0.13
K_2O (wt.%)
SiO_2 (wt.%)
SiO_2 (wt.%)

Figure 6

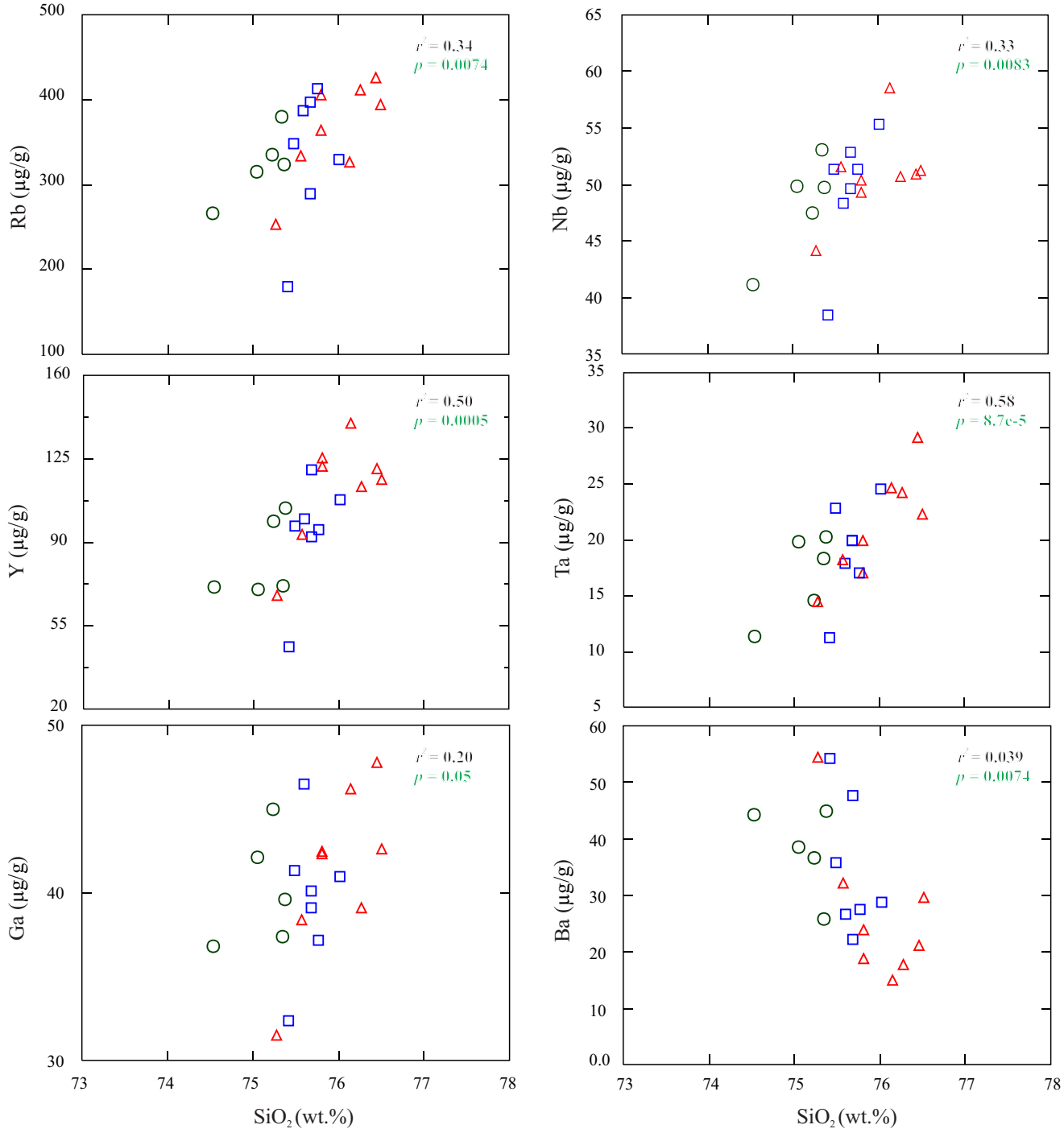
Rb (µg/g)
r^2 = 0.34
p = 0.0074
Nb (µg/g)
r^2 = 0.33
p = 0.0083
Y (µg/g)
r^2 = 0.50
p = 0.0005
Ta (µg/g)
r^2 = 0.58
p = 8.7e-5
Ga (µg/g)
r^2 = 0.20
p = 0.05
Ba (µg/g)
r^2 = 0.039
p = 0.0074
SiO_2 (wt.%)
SiO_2 (wt.%)

Figure 7

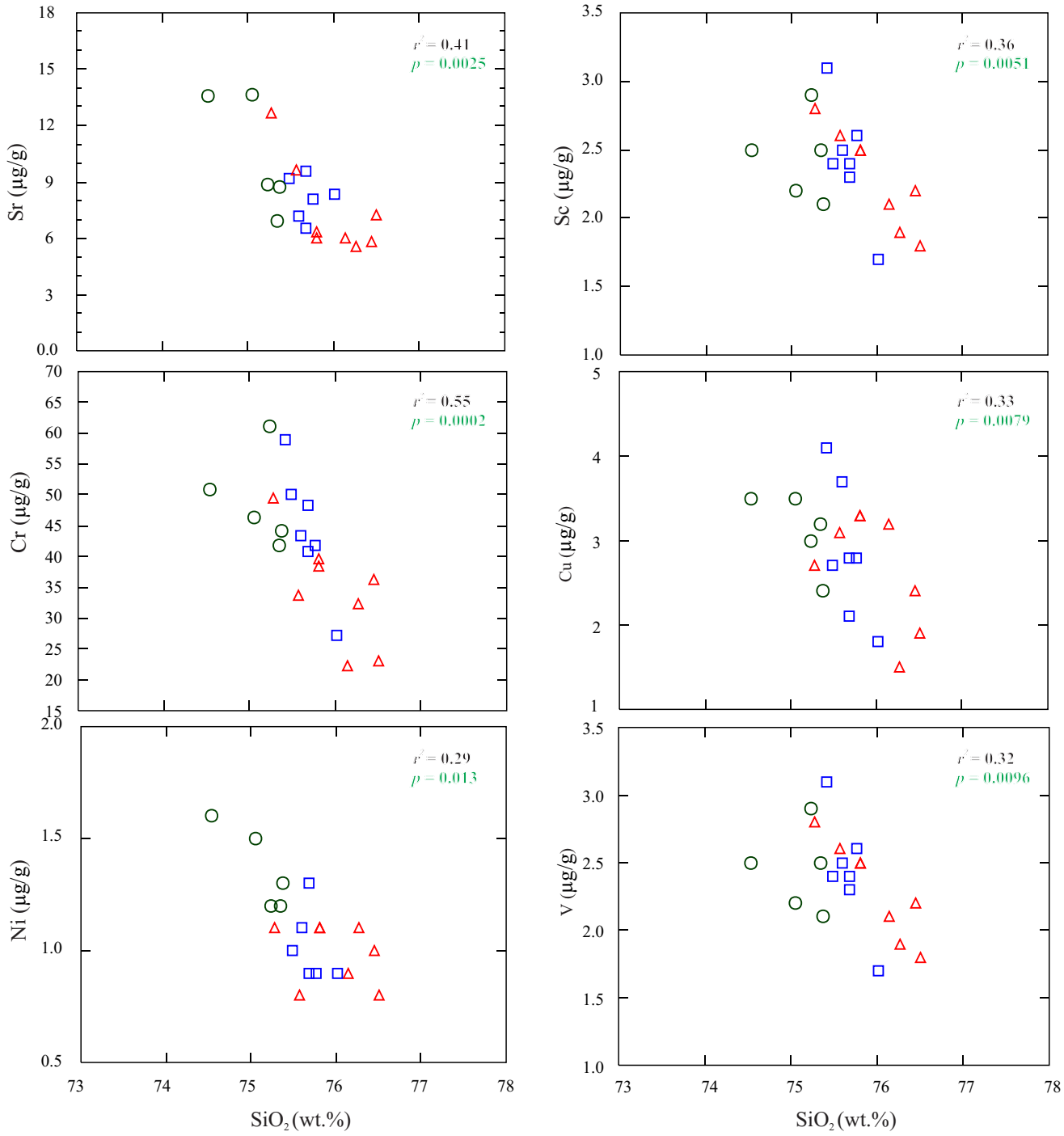

Figure 7 Cont.

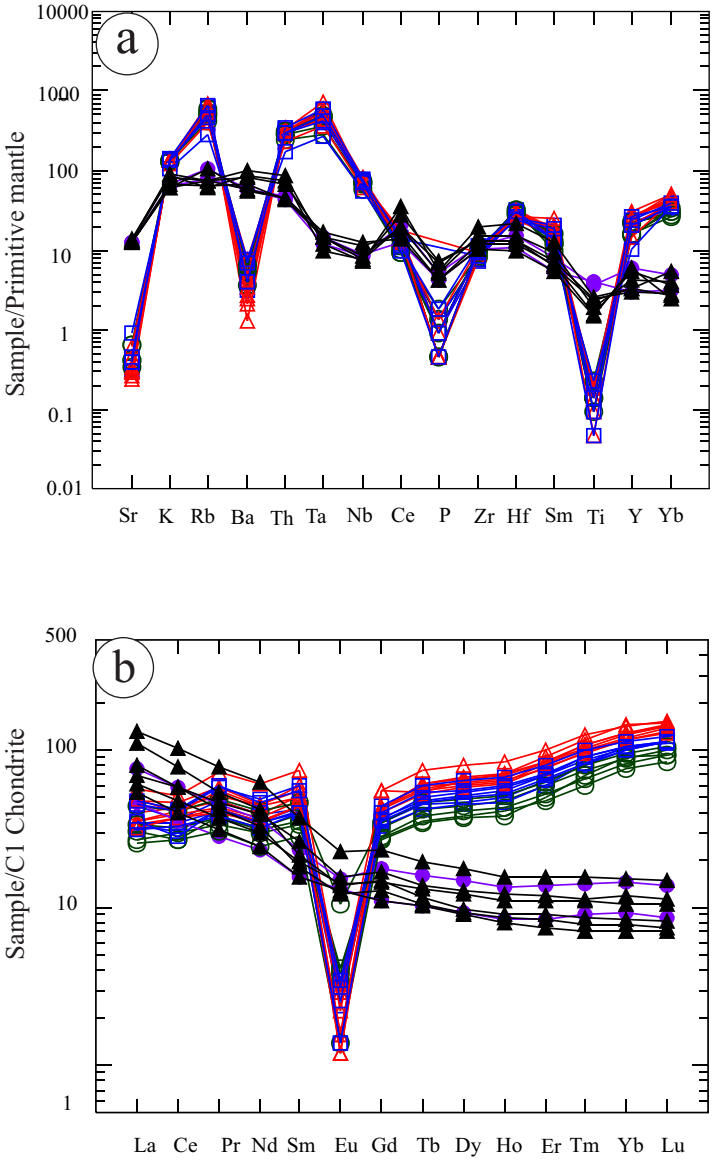
a
Sample/Primitive mantle
10000
1000
100
10
1
0.1
0.01
Sr K Rb Ba Th Ta Nb Ce P Zr Hf Sm Ti Y Yb
b
Sample/C1 Chondrite
500
100
10
1
La Ce Pr Nd Sm Eu Gd Tb Dy Ho Er Tm Yb Lu

Figure 8

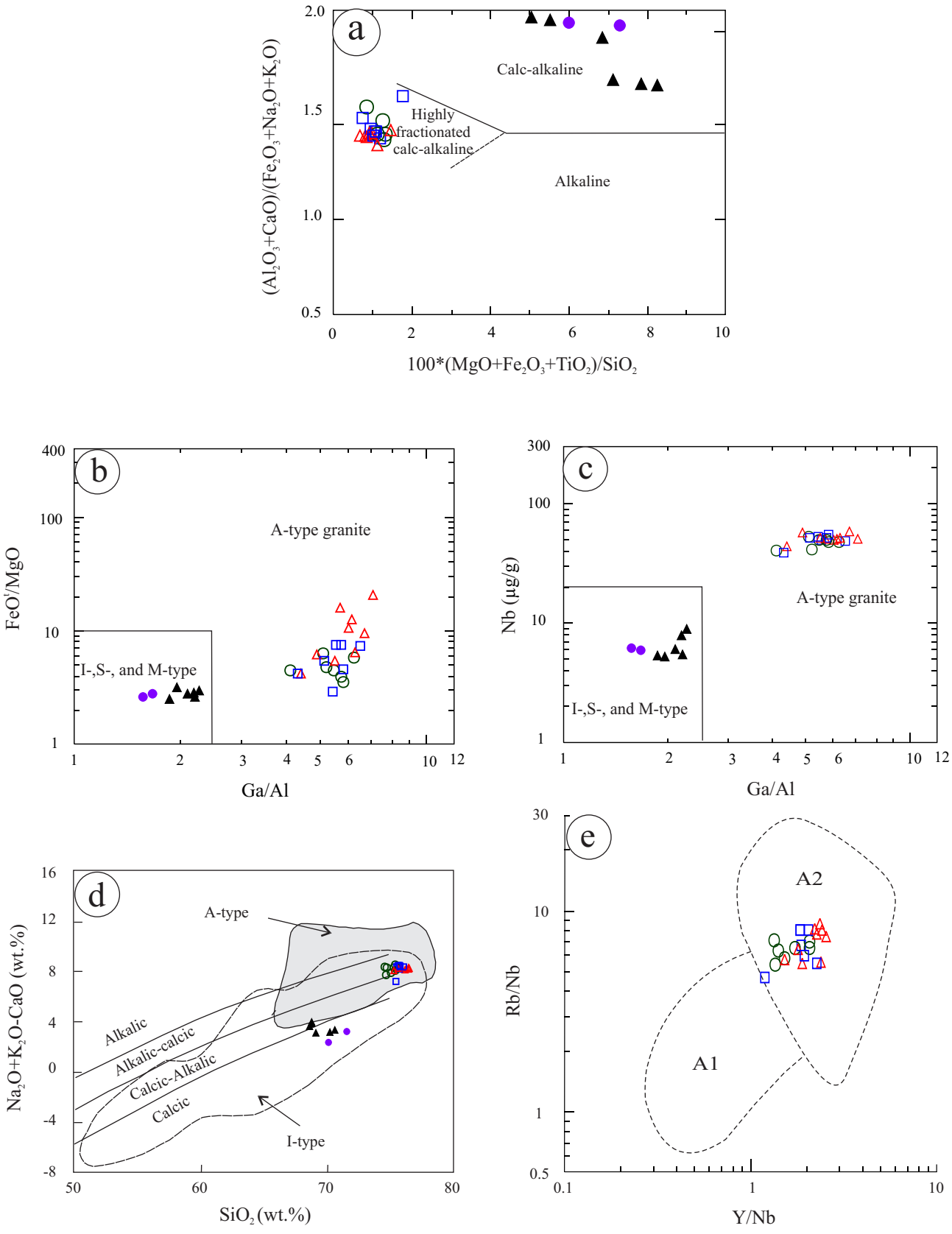
a
Calc-alkaline
Highly fractionated calc-alkaline
Alkaline
(Al2O3+CaO)/(Fe2O3+Na2O+K2O)
100*(MgO+Fe2O3+TiO2)/SiO2
b
A-type granite
I-,S-, and M-type
FeO'/MgO
Ga/Al
c
A-type granite
I-,S-, and M-type
Nb (μg/g)
Ga/Al
d
A-type
Alkalic
Alkalic-calcic
Calcic-Alkalic
Calcic
I-type
Na2O+K2O-CaO (wt.%)
SiO2 (wt.%)
e
A2
A1
Rb/Nb
Y/Nb

Figure 9

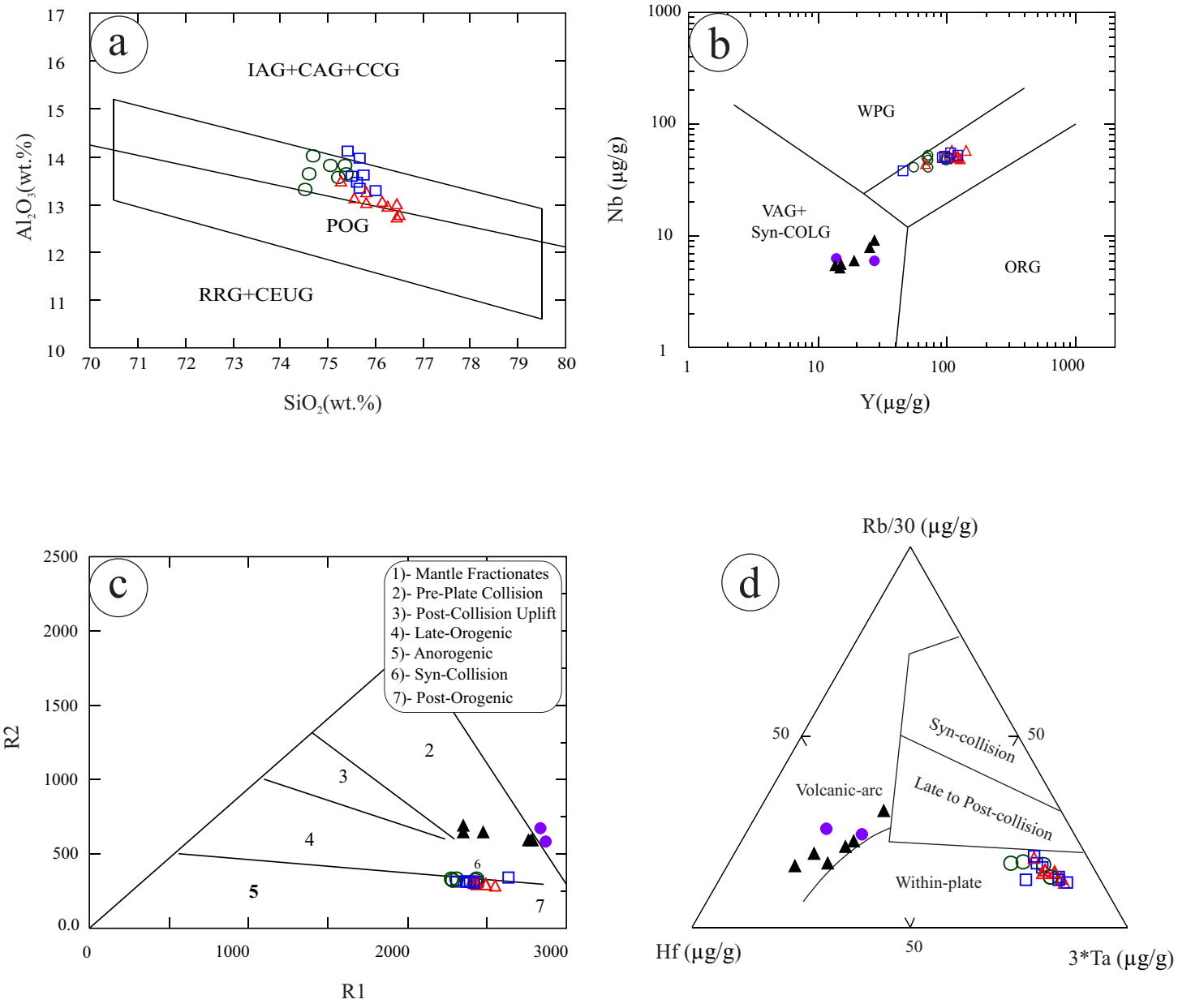
a
IAG+CAG+CCG
POG
RRG+CEUG
Al2O3(wt.%)
SiO2(wt.%)
b
WPG
VAG+
Syn-COLG
ORG
Nb (µg/g)
Y(µg/g)
c
1)- Mantle Fractionates
2)- Pre-Plate Collision
3)- Post-Collision Uplift
4)- Late-Orogenic
5)- Anorogenic
6)- Syn-Collision
7)- Post-Orogenic
R2
R1
d
Rb/30 (µg/g)
Syn-collision
Late to Post-collision
Volcanic-arc
Within-plate
Hf (µg/g)
3*Ta (µg/g)

Figure 10

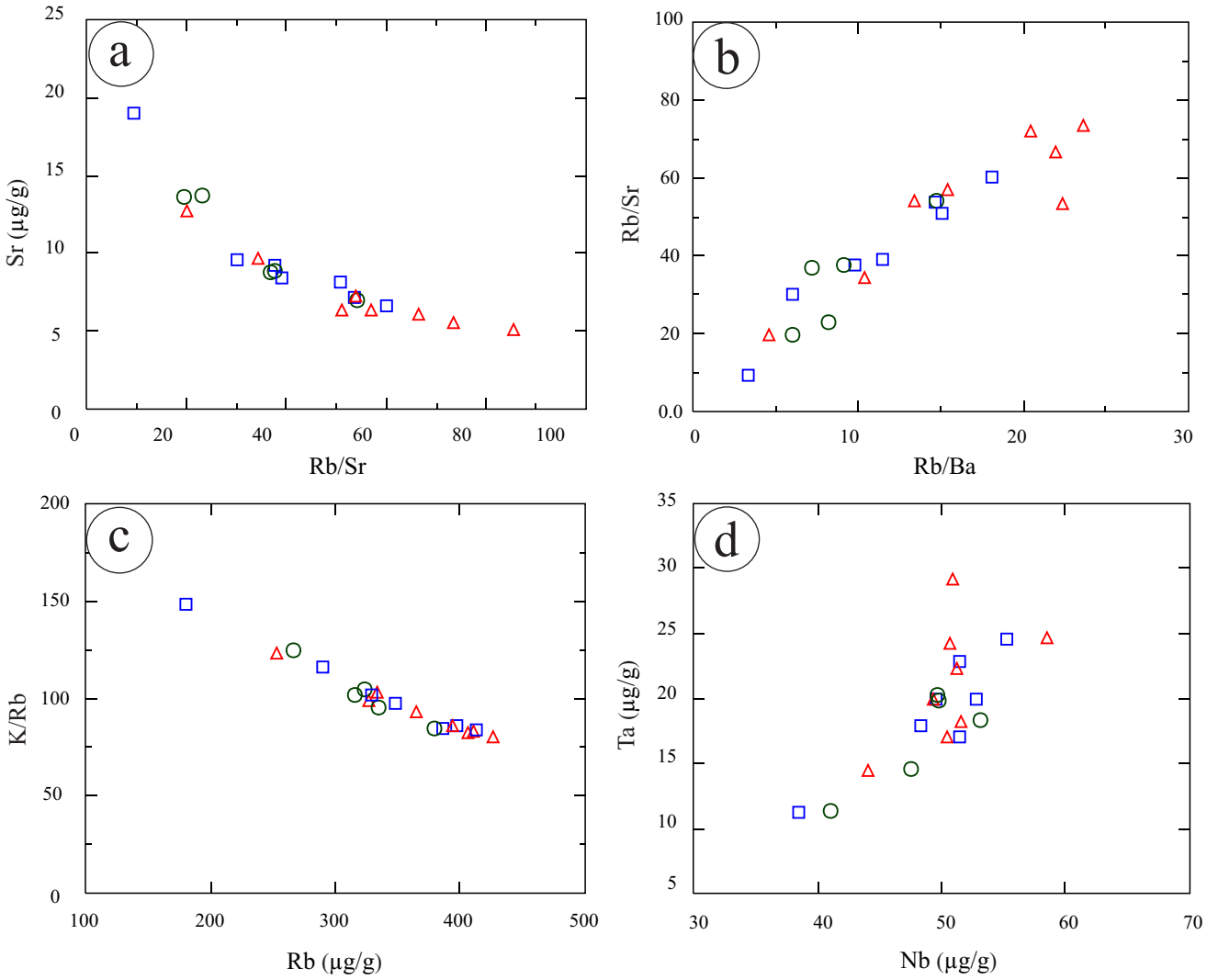

Figure 11

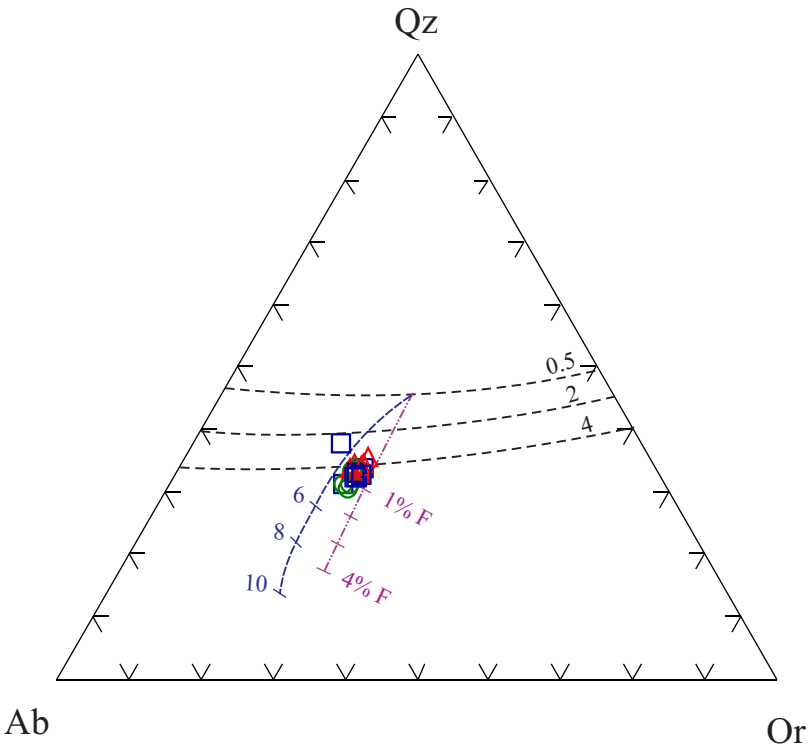

Figure 12

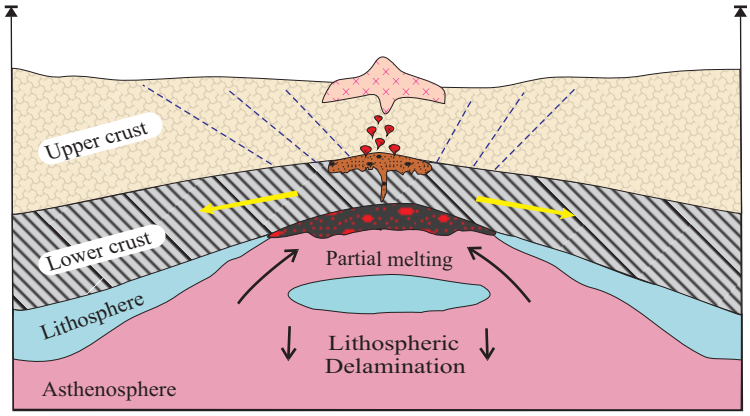
Upper crust
Lower crust
Lithosphere
Partial melting
Lithospheric
Delamination
Asthenosphere

Figure 13